Title

Drosophila model to clarify the pathological significance of OPA1 in autosomal dominant optic atrophy

Authors

Yohei Nitta[1, †], Jiro Osaka[1,2, †], Ryuto Maki[2], Satoko Hakeda-Suzuki[2,3], Emiko Suzuki[4,5], Satoshi Ueki[6], Takashi Suzuki[2] and Atsushi Sugie[1 *]

[1] Brain Research Institute, Niigata University, Niigata, 951-8585, Japan

[2] School of Life Science and Technology, Tokyo Institute of Technology, Yokohama, 226-8501, Japan

[3] Research Initiatives and Promotion Organization, Yokohama National University, Yokohama, 240-8501, Japan

[4] Department of Biological Sciences, Graduate School of Science, Tokyo Metropolitan University, Hachioji 192-0397, Japan

[5] Department of Gene Function and Phenomics, National Institute of Genetics, Mishima, 411-8540, Japan

[6] Division of Ophthalmology and Visual Science, Graduate School of Medical and Dental Sciences, Niigata University, Niigata, 951-8585, Japan

[†] Equal contribution

[*] Corresponding author: atsushi.sugie@bri.niigata-u.ac.jp (A.S.) Tel (+81) 25-227-0616.

Abstract

Autosomal dominant optic atrophy (DOA) is a progressive form of blindness caused by degeneration of retinal ganglion cells and their axons, mainly caused by mutations in the OPA1 mitochondrial dynamin *like* GTPase (*OPA1*) gene. *OPA1* encodes a dynamin-like GTPase present in the mitochondrial inner membrane. When associated with OPA1 mutations, DOA can present not only ocular symptoms but also multi-organ symptoms (DOA plus). DOA plus often results from point mutations in the GTPase domain, which are assumed to have dominant negative effects. However, the presence of mutations in the GTPase domain does not always result in DOA plus. Therefore, an experimental system to distinguish between DOA and DOA plus is needed. In this study, we found that loss-of-function mutations of the *dOPA1* gene in *Drosophila* can imitate the pathology of optic nerve degeneration observed in DOA. We successfully rescued this degeneration by expressing the human *OPA1* (*hOPA1*) gene, indicating that *hOPA1* is functionally interchangeable with *dOPA1* in the fly system. However, mutations previously identified did not ameliorate the *dOPA1* deficiency phenotype. By expressing both WT and DOA plus mutant *hOPA1* forms in the optic nerve of *dOPA1* mutants, we observed that DOA plus mutations suppressed the rescue, facilitating the distinction between loss-of-function and dominant negative mutations in *hOPA1*. This fly model aids in distinguishing DOA from DOA plus and guides initial *hOPA1* mutation treatment strategies.

Introduction

Autosomal dominant optic atrophy (DOA) is a progressive form of blindness characterized by selective degeneration of retinal ganglion cells (RGCs) and the axons that form the optic nerve. Despite being a rare disease with a frequency of 1/12,000 to 1/50,000, DOA is the most commonly diagnosed form of hereditary optic neuropathy. In 2000, *OPA1 mitochondrial dynamin like GTPase (OPA1)* was identified as the causative gene for DOA (Alexander et al., 2000; Delettre et al., 2000).

45 *OPA1* encodes a dynamin-like GTPase located in the inner mitochondrial membrane (Olichon et
46 al., 2002). It has various functions, including mitochondrial fusion, mtDNA maintenance, control of
47 cell death, and resistance to reactive oxygen species (ROS) (Lenaers et al., 2021). The most common
48 pathogenic mutation in *OPA1* is the c.2708-2711 delTTAG deletion (Toomes et al., 2001). Five
49 pathogenic mutations, including the one above, result in a substantial decrease in OPA1 protein in the
50 fibroblasts from affected patients (Zanna et al., 2008), supporting the theory that DOA is caused by
51 haploinsufficiency.

52 Optic atrophy is a characteristic feature of *OPA1*-associated DOA; however, multisystem
53 symptoms have been reported in up to 20% of *OPA1* mutation carriers (Yu-Wai-Man et al., 2010a).
54 This is called DOA plus. DOA plus can include sensorineural deafness (Amati-Bonneau et al., 2008),
55 multiple sclerosis-like illness (Verny et al., 2008; Yu-Wai-Man et al., 2016), parkinsonism and
56 dementia (Carelli et al., 2015; Lynch et al., 2017), and cardiomyopathy (Spiegel et al., 2016). The
57 R445H mutation is a well-known mutation associated with DOA plus (Amati-Bonneau et al., 2008,
58 2003; Shimizu et al., 2003). The proportion of mutated OPA1 locations differs between patients with
59 DOA and DOA plus. Missense mutations in the dynamin-featured structure, especially the GTPase
60 domain of *OPA1*, are more likely to cause severe symptoms compared with loss-of-function (LOF)
61 mutations such as deletions or splice site mutations (Yu-Wai-Man et al., 2010a). This is probably due
62 to the dominant negative effect (DN) of a DOA plus mutation on the normal *OPA1* allele, since OPA1
63 functions as a homo-oligomer (Frezza et al., 2006; Olichon et al., 2006); in fact, its yeast ortholog,
64 Mgm1, forms oligomers, increasing the GTPase activity (Meglei and McQuibban, 2009; Rujiviphat
65 et al., 2009). Particularly, the dynamin-featured structure accounts for 70% of the 233 pathogenic
66 variants of DOA and DOA plus described in the locus-specific database (Ferré et al., 2015). However,
67 mutations in these domains do not determine DOA plus, as it affects only 20% of all *OPA1* mutation
68 carriers. Thus, experimental models to determine whether a gene mutation is LOF or DN are required
69 to distinguish between DOA and DOA plus. Although currently there is no effective treatment for
70 DOA or DOA plus, distinguishing between them allows earlier planning of interventions such as
71 hearing aids, rather than relying solely on visual aids, necessary only for those with DOA plus. In the

quest to differentiate between LOF and DN effects within the context of genetic mutations, precedents exist in simpler systems such as yeast and human fibroblasts. These models have provided valuable insights into the conserved functions of OPA1 across species, as evidenced by studies in yeast models (Del Dotto et al., 2017) and fibroblasts derived from patients harboring *OPA1* mutations (Kane et al., 2017). However, the ability to distinguish between LOF and DN effects in an in vivo model organism, particularly at the structural level of retinal axon degeneration, has remained elusive. This gap underscores the necessity for a more complex model that not only facilitates molecular analysis but also enables the examination of structural changes in axons and mitochondria, akin to those observed in the actual disease state.

As *OPA1* is conserved in various species, DOA models have been reported in vertebrates such as mice and zebrafish, simple organisms such as nematodes and fruit flies, and *in vitro* yeast and cultured cell models (Del Dotto and Carelli, 2021). In mouse models, focal RGC axons decrease in number with mitochondrial abnormalities at the electron microscope level, but the phenotype appears slowly, not allowing for analysis in a short time frame (Alavi et al., 2007; Davies et al., 2007; Nguyen et al., 2011; Sarzi et al., 2012). Zebrafish models have displayed developmental delays in eyes and heads, short length, and body axis abnormalities (Eijkenboom et al., 2019; Rahn et al., 2013) but have not been used to investigate optic nerve degeneration.

In *C. elegans*, most studies focused on muscle cells using mutants of *eat-3*, an *OPA1* homolog (Kanazawa et al., 2008; Rolland et al., 2009). However, the mitochondria in the posterior lateral microtubule neurons did not show any difference in size from its wild-type (WT) counterparts (Byrne et al., 2019). Thus, LOF of *eat-3* may have a limited impact on phenotypic outcomes in the nervous system. Nevertheless, a DOA model in which $hOPA1^{K301A}$ is expressed in GABAergic motor neurons, showed a decreased number of mitochondria in those cells (Zaninello et al., 2020). In a fly model, the *dOPA1* somatic clone in the eye exhibited a rough-eye phenotype, eye structural abnormalities, and increased MitoSOX fluorescence, which was partially rescued by vitamin E or SOD1 expression (Yarosh et al., 2008). Heterozygous *dOPA1* mutants showed shortened lifespan, elevated ROS levels,

98 and irregular muscle tissue mitochondrial structures (Tang et al., 2009). Moreover, the
99 Electroretinogram (ERG) pattern showed age-dependent decreases in the on transient response, heart
100 rate, negative geotaxis response, and increased heart arrhythmia due to heat shock stress (Shahrestani
101 et al., 2009). However, except for mice, the evidence of optic nerve axonal abnormalities is limited in
102 model organisms such as zebrafish, worms, and flies.

103 The structure of the *Drosophila* visual system is similar to that of mammals (Sanes and Zipursky,
104 2010), with conserved mechanisms of synaptogenesis and neural circuit formation (Sanes and
105 Zipursky, 2020). *Drosophila* photoreceptors type R7/8 extend their retinal axons from the retina
106 directly into the brain, forming synapses in the second optic ganglion medulla via the chiasma (Figure
107 1A), having potential application as a model for mammalian photoreceptors and RGCs. In this study,
108 we defined the retinal axons of *Drosophila* as analogous to the human optic nerve. Based on this, we
109 aimed to develop an experimental model for observing and quantifying degeneration in the *Drosophila*
110 retinal axon (Nitta et al., 2023; Richard et al., 2022).

111 In this study, a *dOPA1* LOF could mimic the human DOA, in which mitochondrial fragmentation,
112 increased ROS levels, and neurodegeneration occur in retinal axons. The axonal degeneration induced
113 by the *dOPA1* mutant was rescued by the expression of human *OPA1* (*hOPA1*). This demonstrated that
114 the function of *hOPA1* is the same as in the fly. Previously reported mutations failed to rescue the
115 dOPA1 deficiency phenotype. To distinguish between the effect of LOF and DN mutations, we
116 expressed the *hOPA1* gene of both WT and mutation in a genetic background in which *dOPA1* was
117 deleted in retinal axons. The DOA plus mutations D438V and R445H inhibited the rescue by the WT
118 of *hOPA1*. Taken together, we generated a new *Drosophila* DOA model which served to isolate the
119 LOF or DN effect of *hOPA1* mutations.

120

121 **Results**

122 ***dOPA1* depletion caused mitochondrial fragmentation in axon terminals**

123 The OPA1 protein is located in the inner mitochondrial membrane. To confirm whether dOPA1 is also
124 localized in the mitochondria of *Drosophila* retinal axons, we used a Gal4/UAS system (Brand and
125 Perrimon, 1993) and expressed HA-tagged dOPA1 proteins using the eye-specific *GMR-Gal4* driver
126 (Newsome et al., 2000a, 2000b). The outer membrane of the mitochondria was visualized with
127 mCherry-mito, which tagged the transmembrane domain of Miro with mCherry (Vagnoni and Bullock,
128 2016). Confocal microscopy revealed that the HA signals colocalized with mCherry-mito in the axon
129 terminals of photoreceptor cells (Figure 1B). This indicated that dOPA1 colocalizes with mitochondria
130 in retinal axons.

131 To examine the impact of *dOPA1* on mitochondrial structure and density, we analyzed
132 mitochondria in *dOPA1* RNAi flies. The intensity of the mitochondrial signal was significantly
133 reduced in the retinal axons of these flies (Figure 1C and D; quantification in 1E). Previously, impaired
134 mitochondrial transport was reported in the LOF of *marf* (MFN 1/2 homolog), which is necessary for
135 the fusion of the outer membrane of mitochondria (Sandoval et al., 2014). Thus, we investigated if the
136 LOF of *dOPA1* may cause transport defects, which may be responsible for the reduced mitochondrial
137 density in retinal axons in *dOPA1* RNAi flies. To this end, we observed the photoreceptor neurons
138 after puparium formation at 24 h, which allowed us to simultaneously visualize the cell bodies and
139 axon terminals of the photoreceptors (Figure S1A). Both *dOPA1* knockdown and control flies showed
140 mitochondrial signals in the axon terminals (Figure S1B and C). However, no mitochondrial signals
141 were observed in the axon terminals of flies with a knockdown of *milton*, which is thought to act as
142 an adaptor between kinesin to mitochondria, promoting anterograde transport (Figure S1D). These
143 findings suggest that trafficking defects are not the main cause of the mitochondrial mislocalization
144 observed in the retinal axons of the *dOPA1* knockdown.

145 To further analyze the mitochondrial morphology of retinal axons in the LOF of *dOPA1*, we
146 conducted an electron microscopy analysis (Figure 1F and G). Although *Drosophila* has eight types

147 of photoreceptors, the axons of R1–6, which project to the lamina of the first optic lobe, can be
148 identified without markers; thus, we chose them for this experiment. The *dOPA1* knockdown led to a
149 significant decrease in mitochondria size in R1–6 axons (Figure 1F–H). In addition, there was
150 significant heterogeneity in healthy mitochondria, ranging from dense-matrix (Class A) to swollen
151 mitochondria with a hypodense matrix (Class B) (Figure 1I). Knocking down *dOpa1* in R1–6 axon
152 terminals resulted in severely abnormal mitochondrial ultrastructure (22.8%; Figure 1J). These results
153 suggest that *dOPA1* is involved in maintaining proper mitochondrial morphology by promoting
154 mitochondrial fusion in retinal axons.

155 To verify whether ROS is increased in the retinal axons in *dOPA1* knockdown photoreceptors, we
156 measured the ROS levels in the knockdown retinal axons using MitoSOX, a mitochondrial superoxide
157 indicator (Yarosh et al., 2008). The results showed significantly elevated ROS levels in *dOPA1*
158 knockdown retinal axons compared to control (Figure 2A and B; quantification in 2C).

159 Given that an increase in mitophagy activity has been reported in mouse RGCs and nematode
160 ADOA models (Zaninello et al., 2022, 2020), the mitoQC marker, an established indicator of
161 mitophagy activity, was expressed in the photoreceptors of *Drosophila*. The mito-QC reporter consists
162 of a tandem mCherry-GFP tag that localizes to the outer membrane of mitochondria (Lee et al., 2018).
163 This construct allows the measurement of mitophagy by detecting an increase in the red-only mCherry
164 signal when the GFP is degraded after mitochondria are transported to lysosomes.
165 Post *dOPA1* knockdown, we observed a significant elevation in mCherry positive and GFP negative
166 puncta signals at one week, demonstrating an activation of mitophagy as a consequence
167 of *dOPA1* knockdown (Figure 2D–H).

168

169 **The *dOPA1* LOF leads to progressive distal degeneration of *Drosophila* photoreceptors**

170 We tested whether knocking down *dOPA1* causes optic nerve degeneration in *Drosophila*. To this end,
171 we performed an RNAi experiment using the *GMR-Gal4* driver and evaluated the number of retinal
172 axons projecting to the second optic ganglion medulla (Figure 3A). To compare the number of retinal
173 axon terminals–R7 axons–between genotypes, we used a previously developed automated method,
174 MeDUsA (method for the quantification of degeneration using fly axons) (Nitta et al., 2023). We have
175 assessed the extent of their reduction from the total axonal terminal count, thereby determining the
176 degree of axonal terminal degeneration (Nitta et al., 2023; Richard et al., 2022). Our results showed
177 that the *dOPA1* knockdown caused axonal degeneration one day after eclosion, further decreasing one
178 week later (Figure 3B–E, quantification in 3F). We obtained similar results with an independent
179 alternative RNAi line (Figure S2A and B). To determine whether the degeneration was limited to the
180 axons, we counted the number of rhabdomeres in the cell bodies. Each compound eye comprises 700-
181 800 ommatidia, with each ommatidium containing eight types of photoreceptors, designated as R1–
182 R8. The distal region of an ommatidium reveals the R1–R7 photoreceptors with a stereotypical
183 arrangement of rhabdomeres (arrowheads in Figure 3G–J). Since it is easy to evaluate retinal
184 degeneration by counting the number of rhabdomeres, a decrease in their number indicates
185 degeneration of the photoreceptor cell body. The *dOPA1* knockdown caused a significant decrease in
186 the number of rhabdomeres per ommatidium in 1-week-old adults (Figure 3G–J, quantification in 3K).
187 Interestingly, although the retinal axons had already decreased on the day of eclosion, the ommatidia
188 remained intact (Figure 3F and K). Note that the ommatidia in R7 remained intact after one week
189 (Figure 3J). Our results indicate that the *dOPA1* knockdown causes degeneration in both axonal
190 terminals and cell bodies, with the neuronal degeneration starting from the axons and continuing in
191 the cell bodies. A previous report indicated that the compound eyes of homozygous mutations of
192 *dOPA1* displayed a glossy eye phenotype (Yarosh et al., 2008). Upon knocking down *dOPA1* using the
193 *GMR-Gal4* driver, we also observed a glossy eye-like rough eye phenotype in the compound eyes
194 (Figure S3). The *GMR-Gal4* driver does not exclusively target Gal4 expression to photoreceptor cells.
195 Consequently, the observed retinal axonal degeneration could potentially be secondary to
196 abnormalities in support cells external to the photoreceptors.

197 To test whether our RNAi results reflect *dOPA1* downregulation, we performed mutant analysis of
198 the *dOPA1* gene in retinal axons. For this, we used the *dOPA1*^{s3475} hypomorphic mutant allele, which
199 has a P-element insertion in exon 2 (Yarosh et al., 2008). Somatic mosaic clones were generated in the
200 retinal axons using the FLP/FRT system (Golic and Lindquist, 1989) because homozygous mutant
201 alleles are embryonic lethal (Sandoval et al., 2014; Yarosh et al., 2008). Note that the mutant clone
202 analysis was conducted in a context where mutant and heterozygous cells coexist as a mosaic, and it
203 was not possible to distinguish between them. Using MeDUsA, we found a significantly lower number
204 of *dOPA1* mutant retinal axons than in controls one day after eclosion (Figure 4A and B, quantification
205 in 4D). To determine if *dOPA1* is responsible for axon neurodegeneration, we quantify the number of
206 the axons in the *dOPA1* eye clone fly with the expression of *dOPA1* at one day after eclosion and found
207 that *dOPA1* expression partially rescued the axonal degeneration (Figure 4C, quantification in 4D).
208 Our results indicate that *dOPA1* is necessary for maintaining the number of retinal axons in the
209 *Drosophila* visual system. In conclusion, the neurodegeneration observed in the LOF of *dOPA1* is due
210 to the progressive loss of retinal axons, as well as the mammal optic nerve.

211

212 **Investigating disease mutations in OPA1 using a fly DOA model to confirm their pathological**
213 **significance**

214 Our observations in *dOPA1* LOF flies confirmed mitochondria fragmentation, increased ROS levels,
215 and degeneration of retinal axons, as reported in mammals. These data indicated that the function of
216 *OPA1* may be conserved across *Drosophila* and humans. Thus, we tested whether *hOPA1* could
217 effectively replace *dOPA1* in flies by generating a transgenic organism to express *hOPA1* in
218 *Drosophila*. Following the UAS sequence, that the yeast-derived transcription factor Gal4 binds, the
219 construct included an HA tag, followed by the *hOPA1* gene, and a myc tag (Figure 5A). This construct
220 was expressed in *Drosophila* and protein expression was confirmed by Western blotting. The HA tag,
221 attached to the N-terminus, was immunoblotted resulting in a band of the expected full-length size

222 (Figure 5B). For the myc tag at the C-terminus, a strong band and two weak bands were observed at
223 the upper and lower positions (Figure 5B). Comparison of the expression levels across the variants
224 revealed no significant differences in protein expression (Figure 5C). We also employed a human anti-
225 OPA1 antibody to verify the expression of hOPA1 in vivo in *Drosophila*, detecting both the long and
226 short forms of OPA1, band 2 and band 4 respectively (Figure 5D).

227 Using this *UAS-hOPA1*, we performed rescue experiments. *hOPA1* expression in the retinal axons
228 of the *dOPA1* mutant, which generated somatic cell clones, partially rescued the number of axons
229 (Figure 5E). These results suggest that *hOPA1* and *dOPA1* are interchangeable. We also generated
230 and expressed the *hOPA1* mutation 2708-2711del, which is known to cause DOA, the I382M mutation,
231 located in the GTPase domain and associated with DOA, as well as the D438V and R445H mutations,
232 also located in the GTPase domain and associated with DOA plus. The expression of these mutations
233 in retinal axons failed to rescue the *dOPA1* deficiency to the same extent as the WT *hOPA1* (Figure
234 5E). Importantly, unlike the D438V and R445H mutations, the 2708-2711del and I382M mutations
235 could be weakly rescued. This suggests that these mutations result in LOF, but may retain some
236 residual activity. These findings are also in line with the observed severity of the associated diseases,
237 DOA and DOA plus. As the D438V and R445H mutations were not significantly rescued, unlike the
238 2708-2711del and I382M mutations. Our methodology distinctively facilitates the quantitative
239 evaluation of LOF severity by comparing the rescue capabilities of various mutations. Notably, the
240 2708-2711del and I382M mutations demonstrated only partial rescue, indicative of a hypomorphic
241 effect with residual activity. In contrast, the D438V and R445H mutations failed to show significant
242 rescue, suggesting a more profound LOF. The correlation between the partial rescue by the 2708-
243 2711del and I382M mutations and their classification as hypomorphic is significant. Moreover, the
244 observed differences in rescue efficacy correspond to the clinical severities associated with these
245 mutations, namely in DOA and DOA plus disorders. Thus, our results substantiate the model's ability
246 to quantitatively discriminate among mutations based on their impact on protein functionality,
247 providing an insightful measure of LOF magnitude.

248 Furthermore, we assessed the potential for rescuing ROS signals. Similar to its effect on axonal
249 degeneration, wild-type hOPA1 effectively mitigated the phenotype, whereas the 2708-2711del,
250 D438V, and R445H mutants did not (Figure 5F). Importantly, the I382M variant also reduced ROS
251 levels comparably to the wild type. These findings demonstrate that both axonal degeneration and the
252 increase in ROS caused by dOPA1 downregulation can be effectively counteracted by hOPA1.
253 Although I382M retains partial functionality, it acts as a relatively weak hypomorph in this
254 experimental setup.

255 We also conducted Western blot analyses using anti-COXII and anti-Atg8a antibodies to assess
256 changes in mitochondrial quantity and autophagy activity following the knockdown of *dOPA1*.
257 Mitochondrial protein levels, indicated by COXII quantification, were evaluated to verify
258 mitochondrial content, and the ratio of Atg8a-1 to Atg8a-2 was used to measure autophagy activation.
259 For these experiments, *Tub-Gal4* was employed to systemically knockdown *dOPA1*. Considering the
260 lethality of a whole-body *dOPA1* knockdown, *Tub-Gal80*^{TS} was utilized to repress the knockdown
261 until eclosion by maintaining the flies at 20°C. After eclosion, we increased the temperature to 29°C
262 for two weeks to induce the knockdown or expression of *hOPA1* variants. The results revealed no
263 significant differences across the genotypes tested (Figure S4A–D).

264

265 **Distinction between LOF and DN mutations in *hOPA1* linked to DOA or DOA plus**

266 Currently, the *hOPA1* mutations that contribute to DOA plus have been primarily located in the
267 GTPase domain of *hOPA1*. The role of *hOPA1* as a GTPase is facilitated by its ability to form a
268 polymer via the GED domain and Middle domain (Li et al., 2019). This led to the hypothesis that
269 mutations in the GTPase domain can interact with WT hOPA1 but cannot activate the GTPase activity
270 to show a DN effect. However, it has been challenging to clarify whether these mutations are DN or
271 LOF, as there is a significant number of LOF mutations in the GTPase domain. Given that *dOPA1* can
272 be substituted with *hOPA1*, we suspected that a DN effect could also be achieved by expressing the

273 D438V or R445H mutations in the WT background. However, the axons did not degenerate despite
274 expression and monitoring for two weeks in adult flies (Fig. 6A). The results presented in Figure 5C
275 indicate that there are no significant differences in the expression levels among the variants, suggesting
276 that variations in expression levels do not influence the outcomes. The amino acid sequences of hOPA1
277 and dOPA1 are highly conserved (72% identity), particularly in the GTPase domain. The Middle and
278 GED domains are also relatively well-preserved, with 54% and 64% agreement, respectively (Figure
279 S5). These results imply that, although *dOPA1* and *hOPA1* are functionally interchangeable, they may
280 not interact with each other. Consequently, we expressed *hOPA1* in the photoreceptor depleted of
281 *dOPA1* by somatic clone; under these conditions, we further expressed *hOPA1* WT, 2708-2711del,
282 and mutations in the GTPase domains, including R445H, I382M, and D438V. This allowed *hOPA1*
283 to interact with itself and to verify the DN effect. As a result, the expression of the WT, 2708del, and
284 I382M did not result in any changes when rescued by *hOPA1* substitution (Figure 6B). However, the
285 rescue was significantly suppressed for D438V and R445H, which are known to cause DN; thus, the
286 DN effect could be replicated (Figure 6B). In conclusion, we established an experimental model that
287 can separate LOF and DN, the pathological significance of *hOPA1* mutations. We investigated the
288 impacts of dominant negative mutations on mitochondrial oxidation levels, mitochondrial quantity,
289 and autophagy activation levels; however, none of these parameters showed statistical significance
290 (Figure S6).

291

292 **Discussion**

293 In this study, we found that LOF of *dOPA1* in *Drosophila* can imitate human DOA, in which the optic
294 nerve degenerates. We were successful in reversing this degeneration by expressing *hOPA1* (Figure
295 6C). However, we could not rescue any previously reported mutations known to cause either DOA or
296 DOA plus except for I382M. In the context of rescuing the retinal axons of the *dOPA1* mutant by
297 expressing the WT of *hOPA1*, it was observed that only the DOA plus mutations suppressed the rescue

298 (Figure 6C). This allowed us to distinguish between LOF and DN mutations in *hOPA1*. The fly model
299 developed in this study will allow investigating new *hOPA1* mutations for DOA or DOA plus. We have
300 previously utilized MeDUsA to quantify axonal degeneration, applying this methodology extensively
301 to various neurological disorders. The robust adaptability of this experimental system is demonstrated
302 by its application in exploring a wide spectrum of genetic mutations associated with neurological
303 conditions, highlighting its broad utility in neurogenetic research. We identified a novel de novo
304 variant in Spliceosome Associated Factor 1, Recruiter of U4/U6.U5 Tri-SnRNP (*SART1*). The patient,
305 born at 37 weeks with a birth weight of 2934g, exhibited significant developmental delays, including
306 an inability to support head movement at 7 months, reliance on tube feeding, unresponsiveness to
307 visual stimuli, and development of infantile spasms with hypsarrhythmia, as evidenced by EEG
308 findings. Profound hearing loss and brain atrophy were confirmed through MRI imaging. To assess
309 the functional impact of this novel human gene variant, we engineered transgenic Drosophila lines
310 expressing both wild type and mutant *SART1* under the control of a UAS promoter. Our MeDUsA
311 analysis suggested that the variant may confer a gain-of-toxic-function (Nitta et al., 2023). Moreover,
312 we identified heterozygous loss-of-function mutations in *DHX9* as potentially causative for a newly
313 characterized neurodevelopmental disorder. We further investigated the pathogenic potential of a novel
314 heterozygous de novo missense mutation in *DHX9* in a patient presenting with short stature,
315 intellectual disability, and myocardial compaction. Our findings indicated a loss of function in the
316 G414R and R1052Q variants of *DHX9* (Yamada et al., 2023). This experimental framework has been
317 instrumental in elucidating the impact of gene mutations, enhancing our ability to diagnose how novel
318 variants influence gene function. Our research established that *dOPA1* knockdown precipitates
319 axonal degeneration and elevates ROS signals in retinal axons. Expression of human *OPA1* within
320 this context effectively mitigated both phenomena; it partially reversed axonal degeneration and
321 nearly completely normalized ROS levels. These results imply that factors other than increased
322 ROS may drive the axonal degeneration observed post-knockdown. Furthermore, while
323 differences between the impacts of DN mutations and loss-of-function mutations were evident in
324 axonal degeneration, they were less apparent when using ROS as a biomarker. The extensive use

325 of transgenes in our experiments might have mitigated the knockdown effects. In a systemic
326 *dOPA1* knockdown, assessments of mitochondrial quantity and autophagy activity revealed no
327 significant changes, suggesting that the cellular consequences of reduced *OPA1* expression might
328 vary across different cell types.

329 In our study, expressing *dOPA1* in the retinal axons of *dOPA1* mutants resulted in significant
330 rescue, but it did not return to control levels. There are three possible explanations for this result. The
331 first concerns gene expression levels. The Gal4-line used for the rescue experiments may not replicate
332 the expression levels or timing of endogenous *dOPA1*. Considering that the optimal functionality
333 of *dOPA1* may be contingent upon specific gene expression levels, attaining a wild-type-like state
334 necessitates the precise regulation of these expression levels. The second is a non-autonomous issue.
335 Although *dOPA1* gene expression was induced in the retinal axons for the rescue experiments, many
336 retinal axons were homozygous mutants, while other cell types were heterozygous for
337 the *dOPA1* mutation. If there is a non-autonomous effect of *dOPA1* in cells other than retinal axons, it
338 might not be possible to restore the wild-type-like state fully. The third potential issue is that only one
339 isoform of *dOPA1* was expressed. In mouse OPA1, to completely restore mitochondrial network shape,
340 an appropriate balance of at least two different isoforms, l-OPA1 and s-OPA1, is required (Del Dotto
341 et al., 2017). This requirement implies that multiple isoforms of *dOPA1* are essential for the dynamic
342 activities of mitochondria.

343 Our established fly model is the first simple organism to allow observation of degeneration of the
344 retinal axons. The mitochondria in the axons showed fragmentation of mitochondria. Former studies
345 have observed mitochondrial fragmentation in S2 cells (McQuibban et al., 2006), muscle tissue (Deng
346 et al., 2008), segmental nerves (Trevisan et al., 2018), and ommatidia (Yarosh et al., 2008) due to the
347 LOF of *dOPA1*. Our study presents compelling evidence that *dOPA1* knockdown instigates neuronal
348 degeneration, characterized by a sequential deterioration at the axonal terminals and extending to the
349 cell bodies. This degenerative pattern, commencing from the distal axons and progressing proximally
350 towards the cell soma, aligns with the paradigm of 'dying-back' neuropathy, a phenomenon extensively

351 documented in various neurodegenerative disorders (Wang et al., 2012). Previously, the function of
352 *OPA1* in mice (*mOPA1*) was substituted by *hOPA1* (Del Dotto et al., 2017; Sarzi et al., 2018). Here we
353 demonstrated that the function of *dOPA1* can also be substituted by *hOPA1*. Thus, the function of *OPA1*
354 is conserved across a wide range of species but our fly model has the advantage of allowing rapid
355 observation of phenotypes. In the mouse model of DOA with the heterozygous deletion of the *mOPA1*
356 gene at positions 329–355 (Alavi et al., 2007) or delTTAG mutant (Sarzi et al., 2012), a decrease in
357 the number of RGC was observed after 17 months or 16 months of age, respectively. To save time,
358 using a fly model for quick analysis and direct observation of retinal axons would be useful. Previous
359 models using nematodes, flies, and zebrafish did not observe axonal degeneration directly, but our
360 new model has made this possible. As a result, our model has the potential to be used for screening for
361 modifiers of unclear molecular pathologies and drug screening.

362 Our model could also demonstrate the pathological significance of *hOPA1* mutations and be used
363 for genetic diagnosis to differentiate between LOF and DN mutations. To elucidate the
364 pathophysiological implications of mutations in the *OPA1* gene, we engineered and expressed several
365 human *OPA1* variants, including the 2708-2711del mutation, associated with DOA, and the I382M
366 mutation, located in the GTPase domain and linked to DOA. We also investigated the D438V and
367 R445H mutations in the GTPase domain and correlated with the more severe DOA plus phenotype.
368 The 2708-2711del mutation exhibited limited detectability via HA-tag probing. Still, it was
369 undetectable with a myc tag, likely due to a frameshift event leading to the mutation's characteristic
370 truncated protein product, as delineated in prior studies (Zanna et al., 2008). Contrastingly, the I382M,
371 D438V, and R445H mutations demonstrated expression levels comparable to the WT *hOPA1*.

372 However, the expression of these mutants in retinal axons did not restore the *dOPA1* deficiency to
373 the same extent as the WT hOPA1, as evidenced in Figure 5E. This finding indicates a functional
374 impairment imparted by these mutations, aligning with established understanding (Zanna et al., 2008).
375 Notably, while the 2708-2711del and I382M mutations exhibited limited functional rescue, the D438V
376 and R445H mutations did not show significant rescue activity. This differential rescue efficiency

377 suggests that the former mutations, particularly the I382M, categorized as a hypomorph (Del Dotto et
378 al., 2018), may retain partial functional capacity, indicative of a LOF effect but with residual activity.
379 The I382M missense mutation within the GTPase domain of OPA1 has been described as a mild
380 hypomorph or a disease modifier. Intriguingly, this mutation alone does not induce significant clinical
381 outcomes, as evidenced by multiple studies (Bonifert et al., 2014; Bonneau et al., 2014; Carelli et al.,
382 2015; Schaaf et al., 2011). A significant reduction in protein levels has been observed in fibroblasts
383 originating from patients harboring the I382M mutation. However, mitochondrial volume remains
384 unaffected, and the fusion activity of mitochondria is only minimally influenced (Del Dotto et al.,
385 2018; Kane et al., 2017). This observation is consistent with findings reported by de la Barca et al.
386 (Chao De La Barca et al., 2020), where a targeted metabolomics approach classified I382M as a mild
387 hypomorph. In our current study, the I382M mutation preserves more OPA1 function compared to DN
388 mutations, as depicted in Figures 5E and F. Considering the results from our *Drosophila* model and
389 previous research, we hypothesize that the I382M mutation may constitute a mild hypomorphic variant.
390 This might explain its failure to manifest a phenotype on its own, yet its contribution to increased
391 severity when it occurs in compound heterozygosity.

392 Our results for LOF or DN segmentation were consistent with previously reported yeast models
393 (Del Dotto et al., 2018) and fibroblasts obtained from patients with OPA1 mutations (Kane et al., 2017),
394 and confirmed the conserved function of *OPA1* across species. A major advantage of the *Drosophila*
395 model over yeast or fibroblasts, is that we can observe a phenotype that mimics the actual disease state
396 of axonal degeneration in retinal axons and analyze it not only at the molecular level, but also the
397 structural level of axons and mitochondria. The transgenic *Drosophila* of disease-associated *hOpa1*
398 mutations created in this study can also serve to understand the pathophysiology of these mutations.

399 Advances in genome analysis allowed the identification of many variants and genetic mutations
400 associated with DOA using next-generation sequencing. This could confirm diagnoses and identify
401 new forms of DOA. The widespread use of these sequencers has also created new challenges, such as
402 the growing number of variants of unknown significance (VUS) in publicly available databases such

403 as CliniVar for DOA. These variants are categorized as pathogenic, likely pathogenic, VUS, likely
404 benign, or benign, and the number of VUS is increasing as more variants are registered. The ClinVar
405 database had classified 110 out of 319 *Opa1* variants as VUS at the end of 2019. By the end of 2022,
406 this number had increased to 357 out of 840, indicating an increase from 34% to 42% over the last
407 three years (Henrie et al., 2018). This trend suggests that the number of VUS in *Opa1* may continue
408 to increase in the future. Analyzing VUS requires testing the effects of a mutation *in vitro* or *in vivo*;
409 this can be expensive and time-consuming without prior confirmation or high probability of
410 pathological significance. However, our fly model can be used to easily and inexpensively determine
411 the pathological effects of disease-causing gene mutations among the growing number of rare
412 mutations identified in DOA.

413 In this study, we tested the effect of expressing the D438V and R445H mutations in the *dOPA1*
414 background and found that retinal axons did not degenerate. Regarding the interactions among OPA1
415 proteins, in yeast Mgm1, K854 in the region near the C-terminus is important for aggregation, and it
416 becomes an oligomer to increase the activity of GTPase (Rujiviphat et al., 2009). Although hOPA1
417 normally has low GTPase activity, its interaction with negatively charged phospholipids such as
418 cardiolipin causes hOPA1 to aggregate, increasing GTP hydrolysis activity (Ban et al., 2010). In the
419 thermophilic fungus *Chaetomium thermophilum*, Mgm1 forms a dimer and then a tetramer at the C-
420 terminal Stalk domain of Mgm1 (Faelber et al., 2019). Structural analysis also predicted that the
421 Middle and GED domains are necessary for dimer and oligomer formation in hOPA1 (Li et al., 2019).
422 In addition, peptide-binding assays have revealed that the coiled-coil domain, which is part of the GED
423 domain, is required for hOPA1 interactions (Akepati et al., 2008). Comparing the amino acid
424 sequences of hOPA1 and dOPA1, the Middle and GED domains, which are necessary for interactions
425 between OPA1 molecules, exhibit concordance rates of 54.3% and 63.6%, respectively. These
426 percentages are low compared to the 71.8% identity observed in the GTPase domains. These suggest
427 that the OPA1 homologs of each species form oligomers with their unique OPA1. Note that the
428 expression of $dOPA1^{K273A}$, a presumably GTPase-negative form of *dOPA1* (Tsuyama et al., 2017),
429 degenerated retinal axons (Figure S7). These results imply that, while dOPA1 and hOPA1 are

430 interchangeable, they may not interact with each other. This could pave the way for the development
431 of a chimeric hOPA1, which would retain its functional properties while avoiding the interaction with
432 endogenous hOPA1. Such chimeric hOPA1 could potentially be used as gene therapy since induced
433 pluripotent stem cells have been generated from a patient with R445H (Sladen et al., 2021).

434 OPA1 has been implicated in various other diseases as well, including normal tension glaucoma
435 (Powell et al., 2003; Yu-Wai-Man et al., 2010b), multiple sclerosis-like illness (Verny et al., 2008;
436 Yu-Wai-Man et al., 2016), Parkinson's disease and dementia (Carelli et al., 2015; Lynch et al., 2017),
437 and cardiomyopathy (Spiegel et al., 2016). Although the connection between these diseases and OPA1
438 is not fully understood, further research on DOA may provide a deeper insight into this relationship.
439 In the future, pathological analysis using the present model could have implications for understanding
440 the mechanisms underlying these diseases.

441 DOA has also been reported to involve mitochondrial DNA (mtDNA) depletion (Amati-Bonneau
442 et al., 2008), but our model, while useful for nuclear gene analysis, is limited for mtDNA analysis.
443 The gene content in the *Drosophila* mtDNA genome is similar as that in vertebrates, but the gene order
444 and distribution on both DNA strands differ. mOPA1 interacts with mtDNA nucleoids through exon
445 4b binding to mtDNA D-loops, independent of mitochondrial fusion (Yang et al., 2020). However,
446 the homologous region of mOPA1 or hOPA1 to exon4b is not found in *Drosophila*, and the D-loop of
447 mtDNA has not been found in cultured cells of flies or in mtDNA of embryos using electron
448 microscopy (Rubenstein et al., 1977). In addition, while the D-loop is involved in mtDNA replication
449 in humans (Fish et al., 2004), the A + T region is the origin of replication in mtDNA replication in
450 *Drosophila* (Goddard and Wolstenholme, 1978). Thus, there may be differences in the mechanism of
451 mtDNA replication between humans and flies (Garesse and Kaguni, 2005). Therefore, the association
452 of dOPA1 with mtDNA may differ from that in mammals and the regulatory mechanism of mtDNA
453 homeostasis in which dOPA1 is involved requires further investigation.

454 Another limitation of our model is that the molecular mechanisms underlying the formation of
455 long-form OPA1 (L-OPA1) and short-form OPA1 (S-OPA1), which are well analyzed in mammals
456 (MacVicar and Langer, 2016), have not been elucidated in *Drosophila*. In hOPA1, S1 or S2 sites are
457 processed by the i-AAA protease OMA1 and Yme1L respectively to produce S-hOPA1 (Anand et al.,
458 2014). Despite the fact that Yme1L is conserved in *Drosophila*, it has been involved in the degradation
459 of the dOPA1 protein rather than its cleavage by dYme1L (Liu et al., 2020). Moreover, the cleavage
460 site for i-AAA does not exist in dOPA1 (Olichon et al., 2007). Regarding other proteases, yeast Mgm1
461 is processed by the rhomboid protease Pcp1 (Esser et al., 2002; Herlan et al., 2003). However, the
462 Rhomboid-7, a Pcp1 ortholog of *Drosophila*, was not required for dOPA1 processing (Whitworth et
463 al., 2008). Although hOPA1 expression in *Drosophila* has identified three different sizes of hOPA1 in
464 our Western blotting result, it is unclear how they are cleaved. From a size perspective, the upper band
465 was inferred to represent the full-length hOPA1 including the mitochondria import sequence (MIS).
466 Since the Middle and the lowest bands were not present in HA-tagged samples, it is possible that the
467 bands at the Middle size represent the long-form hOPA1 (L-hOPA1) in which probably MIS was
468 processed. The band detected at the lowest position may represent a short form of hOPA1 (S-hOPA1).
469 However, *Drosophila* does not have OMA1, an i-AAA protease that cleaves the S1 site. Although
470 another i-AAA protease that cleaves the S2 site, YME1L, is conserved, our expressed hOPA1 is
471 isoform 1 and lacks the S2 site (Fig. 5A). Therefore, it is not clear how S-hOPA1 is processed in
472 *Drosophila*. The anti-dOPA1 antiserum detects three bands in the overexpression of a FLAG-tagged
473 dOPA1 construct (Poole et al., 2010), suggesting a molecular mechanism by which dOPA1, like yeast
474 and mammals, is cleaved after translation. However, the proteases involved in the mechanism are not
475 yet clarified. Whether *Drosophila's* endogenous mechanisms can be used to study how L-OPA1 and
476 S-OPA1 are involved in DOA remains unclear.

477 In this study, we established a new model of DOA in *Drosophila*, in which we discovered the
478 following: 1. We could replicate the human disease of optic nerve degeneration, allowing rapid genetic
479 disease analysis. 2. We could distinguish the LOF and DN effects of *hOPA1* by observation of axonal
480 degeneration phenotype but not with ROS signal, autophagy activity, and amount of the mitochondria

481 in this model. These findings can reveal the pathological significance of *de novo* mutations and are
482 useful in diagnosing DOA or DOA plus. Additionally, while *hOPA1* is the major gene involved in
483 DOA, other genes involved in DOA and interacting proteins have not been investigated yet. Our model
484 can be used for pathological modifier screening, exploring modifiers, and contributing to drug
485 development. In the future, we hope to provide insights that can be applied to the fundamental
486 treatment of DOA.

487

488 **Materials and Methods**

489 ***Fly strains***

490 Flies were maintained at 25°C on standard fly food. For knockdown experiments (Figures 1C–E,
491 1F–J, 2A–H, 3B–K, 5F, S1, S2, S6A, and S7), flies were kept at 29°C in darkness. Female flies
492 were used in all experiments to ensure consistency in the number of retinal axons. The following fly
493 strains were obtained from the Bloomington Drosophila Stock Center (BDSC): *GMR-Gal4* (BDSC
494 1104), *Tub-Gal4* (BDSC 5138), *UAS-dicer2(III)* (BDSC 24651), *UAS-mito-HA-GFP* (BDSC 8443),
495 *UAS-mCherry-mito* (BDSC 66532), *UAS-mitoQC* (BDSC 91641), *UAS-dOPA1 RNAi* (BDSC 32358),
496 *UAS-Milton RNAi* (BDSC 44477), *FRT42D, GMR-hid, l(2)cl-R11[1]/CyO; ey-Gal4, UAS-flp* (BDSC
497 5251), *ey3.5-flp* (BDSC 35542), *Tub-Gal80^{TS}* (BDSC 7017), and *UAS-luciferase RNAi* (BDSC 31603).
498 The following fly strains were obtained from the Vienna Drosophila Resource Center (VDRC): The
499 *40D-UAS* (VDRC 60101) and *UAS-dOPA1 RNAi* (VDRC 106290). The following fly strains were
500 obtained from the Kyoto Drosophila Stock Center (Kyoto): *FRT19* (Kyoto 101231), *FRT42D* (Kyoto
501 101878), and *dOPA1^{s3475}* (Kyoto 111438). The *UAS-dOPA1-HA* and *UAS-dOPA1-HA^{K273A}* were
502 generously provided by T. Uemura (Kyoto University, Japan). The *dOPA1* clone analysis was
503 performed by inducing flippase expression in the eyes using either *ey-Gal4* with *UAS-flp* or *ey3.5-flp*,
504 followed by recombination at the chromosomal location *FRT42D* to generate a mosaic of cells
505 homozygous for *dOPA1^{s3475}*.

506

507 ***Generation of transgenic flies***

508 The cDNA for WT, I382M, D438V, R445H, and 2708-2711del forms of *hOPA1* [NM_015560.3] were
509 generated by Vectorbuilder Inc. (Yokohama, Japan). Then, the HA-hOPA1-myc sequence was
510 amplified and inserted into pJFRC81-10XUAS-IVS-Syn21-GFP-p10 (ID36432, Addgene, USA)
511 digested with *NotI* and *XbaI* using primers with the N-terminal containing the Kozak and HA
512 sequences (TTACTTCAGGCGGCCGCGGCCAAAATGTACCCATACGATGTTCCAGATTAC) and
513 the C-terminal containing the myc sequence
514 (TTAAAAACGATTCATTCTAGTTACAGATCCTCTTCTGAGATGAGTTTTTGTTCTTTCTCCT
515 GATGAAGAGCTTCAATG). To confirm production of the complete coding sequence, it was
516 bidirectionally sequenced using the Sanger method. These plasmids were injected into embryos and
517 integrated into the attP2 landing site via ΦC31 recombination (WellGenetics, Taiwan).

518

519 ***Immunohistochemistry and imaging***

520 Immunohistochemistry was performed as described previously (Sugie et al., 2017). Flies were
521 anesthetized on a CO2 pad, and specimens of the correct genotype were selected. Specimens were
522 briefly washed in ethanol for a few seconds before being transferred to a Petri dish containing
523 phosphate-buffered saline (PBS). Using forceps, the proboscis was secured, and the right and left eyes
524 were dissected out with another set of forceps. The proboscis and attached trachea were also removed
525 from the brain. The brains were then carefully transferred with forceps into a 1.5 mL tube containing
526 150 μL of 0.3% PBT (PBS with Triton-X100) at room temperature.

527 To fix the tissues, 50 μL of 16% formaldehyde was added to each tube, followed by gentle mixing.
528 The samples were incubated in the fixative for 50 minutes at room temperature. Subsequent washing

529 involved three rinses with 200 μL of 0.3% PBT, using a micropipette for fluid exchange. After the
530 final wash, the PBT was removed, and the samples were incubated in the primary antibody solution
531 overnight (O/N) at 4 °C. This was followed by three washes with 0.3% PBT, after which the secondary
532 antibody solution (diluted in 0.3% PBT) was added, and samples were incubated overnight in the dark
533 at 4 °C. After another three washes in 0.3% PBT, the samples were prepared for imaging. The
534 following antibodies were used: rat anti-HA (3F10, 1:400; Roche, Switzer land), mouse anti-Chaoptin
535 (24B10, 1:25; Developmental Studies Hybridoma Bank, USA), rat anti-CadN (DN-Ex#8, 1:50;
536 Developmental Studies Hybridoma Bank), anti-rat Alexa Fluor 488 (1:400; Thermo Fisher Scientific,
537 USA), anti-mouse Alexa Fluor 488 (1:400; Thermo Fisher Scientific), anti-mouse Alexa Fluor 568
538 (1:400; Thermo Fisher Scientific), and anti-rat Alexa Fluor 633 (1:400; Thermo Fisher Scientific).
539 Specimens were mounted using a Vectashield mounting medium (Vector Laboratories, USA). Images
540 were captured using an FV3000 confocal microscope (Olympus, Japan) or a C2 (Nikon, Japan)
541 confocal microscope for Figure S1 and processed using the IMARIS software (Oxford Instruments,
542 UK) or Fiji software, an open-source image analysis software (Schindelin et al., 2012).

543

544 ***Electron microscopy***

545 Fly heads were fixed overnight with 2.5% glutaraldehyde and 2% paraformaldehyde in 0.1 M sodium
546 cacodylate buffer. Heads were then post-fixed with 1% osmium tetroxide, dehydrated in ethanol, and
547 embedded in Epon. Ultra-thin tangential sections of the laminas (70 nm) were stained with uranyl
548 acetate and lead citrate. Random retinas or lamina sections were imaged at a magnification of ×100 k
549 with a VELETA CCD Camera (Olympus) mounted on a JEM 1010 transmission electron microscope
550 (JEOL, Japan). In the R1–6 axons of the lamina, the areas corresponding to mitochondria were
551 quantified using the freehand line tool in NIS Elements software (Nikon). Concurrently, mitochondria
552 were manually categorized based on their structural characteristics: those with a densely packed matrix
553 were classified as Class A, and those with a collapsed structure as Class B.

554

555 ***Quantification of Mito-GFP intensity in retinal axons and retina***

556 To measure the relative intensity of Mito-GFP in the photoreceptor R7/8 axons of the medulla, the
557 imaging analysis software IMARIS was used. First, the M1–6 layers of the medulla, including the
558 R7/8 axons, were manually covered using the surface function. Then, the surface area was masked,
559 the surface of the left axons was stained with anti-Chaoptin, and the Mito-GFP signal was generated
560 automatically using the surface function. Finally, the voxel number of the Mito-GFP surface was
561 divided by the voxel number of the R axon surface. These quantifications were performed by
562 experimenters blind to the genotype.

563

564 ***Mitochondrial superoxide detection and quantification***

565 The ROS level was determined using the MitoSOX Red Mitochondrial Superoxide Indicator (Thermo
566 Fisher Scientific). The procedure involved dissecting adult brains in phosphate-buffered saline (PBS),
567 transferring them to 5 μM MitoSOX solution, and incubating them for 10 min in the dark at room
568 temperature. The brains were then washed with PBS containing 20% Vectashield (Vector Laboratories),
569 followed by sequential washes with PBS containing 40% and 60% Vectashield. The samples were
570 mounted in Vectashield and scanned using an FV3000 confocal microscope (Olympus). To quantify
571 the ROS level in photoreceptor R7/8 axons, the IMARIS software (Bitplane) was used for imaging
572 analysis. The software generated automatic surfaces of the MitoSOX and Mito-GFP signals. Then, the
573 ROS level was calculated by dividing the voxel number of the MitoSOX surface on the Mito-GFP
574 surface by the voxel number of the Mito-GFP surface. These quantifications were performed by
575 experimenters blind to the genotype.

576

577 ***Measurement of mitophagy levels in retinal axons***

578 The mitophagy levels in the photoreceptor R7/8 axons of the medulla were analyzed using the mitoQC
579 reporter. Mitolysosomes were identified by referencing the red-only mCherry puncta of mitoQC. The
580 number of mitolysomes of each voxel image was manually quantified with IMARIS software
581 (Bitplane). These quantifications were performed by experimenters blind to the genotype.

582

583 ***Western blot analysis of the whole Drosophila body***

584 We regulated protein expression temporally across the whole body using the *Tub-Gal4* and *Tub-*
585 *GAL80^{TS}* system. Flies harboring each *hOPA1* variant were maintained at a permissive
586 temperature of 20°C, and upon emergence, females were transferred to a restrictive temperature
587 of 29°C for subsequent experiments. The flies were collected in plastic tubes and sonicated (2 x 30
588 s) using a Q55 sonicator (Qsonica, Newtown, CT, USA) in lysis buffer (10 mM Tris–HCl, pH 7.5, 150
589 mM NaCl, 1 mM EDTA, 2% DDM: 10μl/mg flies) supplemented with 1:1000 (v/v) Protease Inhibitor
590 Cocktail Set III (Calbiochem, USA). Rat anti-HRP-conjugated-HA (3F10, 1: 3000; proteintech,
591 Germany), mouse anti-myc (9B11, 1: 10000; Cell Signaling Technology, USA), rabbit anti-OPA1
592 (ab42364, 1: 1000; Abcam, UK), rabbit anti-COXII (1: 100; Murari et al. *JCB* 2020), rabbit anti-Atg8a
593 (ab109364, 1: 8000; Abcam), mouse anti-α-Tubulin (T9026, 1:100,000; Sigma‐Aldrich, USA),
594 goat HRP-conjugated anti-mouse IgG (SA00001-1, 1: 10,000; proteintech), and goat HRP-conjugated
595 anti-rabbit IgG (7074S, 1: 5,000; Cell Signaling Technology) antibodies were used for Western
596 blotting.

597

598 ***Pairwise alignment of hOPA1 and dOPA1***

599 The amino acid sequences for hOPA1 and dOPA1 were referenced from NM_015560.3 and

NM_166040.2, respectively, and aligned using the EMBOSS Needle (Rice et al., 2000). The GTPase, Middle, and GED domains in dOPA1 were identified by cross-referencing the previously described amino acid positions of these domains in hOPA1 (Liesa et al., 2009). The degree of identity between the aligned amino acid sequences was subsequently determined.

Experimental design and statistical analyses

Experimental analyses were performed using Prism 9 (GraphPad Software, USA). For Figures 1E, 1H, 2C, S2B and S7B, data were analyzed using t tests (and nonparametric tests) and Mann-Whitney tests. For Figure 1J, Fisher's exact test was used. For Figures 2H, 3F, 3K, 4D, 5C, 5E, 5F, 6A, 6B, S3B, S4B, S4D, S6C and S6E, differences among multiple groups were examined using the Kruskal−Wallis test followed by the two-stage linear step-up procedure of Benjamini, Krieger, and Yekutieli tests. The null hypothesis was rejected at a 0.05 level of significance. Sample sizes are indicated in each figure. The number of retinal axons and rhabdomeres, the intensity of Mito-GFP and MitoSOX, the mitochondrial area and the classification, and the corrected *P* values are described in the Results section. All data are expressed as the mean ± SEM.

Acknowledgements

We would like to thank Dr. Uemura for providing us with the transgenic fly strain and Dr. Owusu-Ansah for gifting us the antibody. The Ministry of Education, Culture, Sports, Science, and Technology of Japan (#18K14835, #18J00367 and #21K15619 to Y.N., #21K06184 to S.H.S., #16H06457, #21H02483 and 21H05682 to T.S., #17H04983, #19K22592 and #21H02837 to A.S.), the Japan Agency for Medical Research and Development (AMED) (#JP22ek019484s) to A.S., NIG–JOINT to E.S., Takeda Science Foundation Takeda Visionary Research Grant to T.S., Takeda Science Foundation Life Science Research Grant to A.S., and GSK Japan Research Grant 2022 [AS2021A000166849] to

624 A.S..

625

626 ***References***

627 Akepati VR, Müller EC, Otto A, Strauss HM, Portwich M, Alexander C. 2008. Characterization of OPA1
628 isoforms isolated from mouse tissues. *J Neurochem* **106**:372–383. doi:10.1111/j.1471-
629 4159.2008.05401.x

630 Alavi M V., Bette S, Schimpf S, Schuettauf F, Schraermeyer U, Wehrl HF, Ruttiger L, Beck SC, Tonagel
631 F, Pichler BJ, Knipper M, Peters T, Laufs J, Wissinger B. 2007. A splice site mutation in the murine
632 Opa1 gene features pathology of autosomal dominant optic atrophy. *Brain* **130**:1029–1042.
633 doi:10.1093/brain/awm005

634 Alexander C, Votruba M, Pesch UEA, Thiselton DL, Mayer S, Moore A, Rodriguez M, Kellner U, Leo-
635 Kottler B, Auburger G, Bhattacharya SS, Wissinger B. 2000. OPA1, encoding a dynamin-related
636 GTPase, is mutated in autosomal dominant optic atrophy linked to chromosome 3q28. *Nat Genet*
637 **26**:211–215. doi:10.1038/79944

638 Amati-Bonneau P, Odent S, Derrien C, Pasquier L, Malthiéry Y, Reynier P, Bonneau D. 2003. The
639 association of autosomal dominant optic atrophy and moderate deafness may be due to the R445H
640 mutation in the OPA1 gene. *Am J Ophthalmol* **136**:1170–1171. doi:10.1016/S0002-9394(03)00665-
641 2

642 Amati-Bonneau P, Valentino ML, Reynier P, Gallardo ME, Bornstein B, Boissière A, Campos Y, Rivera
643 H, De La Aleja JG, Carroccia R, Iommarini L, Labauge P, Figarella-Branger D, Marcorelles P, Furby
644 A, Beauvais K, Letournel F, Liguori R, La Morgia C, Montagna P, Liguori M, Zanna C, Rugolo M,
645 Cossarizza A, Wissinger B, Verny C, Schwarzenbacher R, Martín MÁ, Arenas J, Ayuso C, Garesse
646 R, Lenaers G, Bonneau D, Carelli V. 2008. OPA1 mutations induce mitochondrial DNA instability
647 and optic atrophy "plus" phenotypes. *Brain* **131**:338–351. doi:10.1093/brain/awm298

648 Anand R, Wai T, Baker MJ, Kladt N, Schauss AC, Rugarli E, Langer T. 2014. The i-AAA protease YME1L
649 and OMA1 cleave OPA1 to balance mitochondrial fusion and fission. *J Cell Biol* **204**:919–929.

650 doi:10.1083/jcb.201308006

651 Ban T, Heymann JAW, Song Z, Hinshaw JE, Chan DC. 2010. OPA1 disease alleles causing dominant optic
652 atrophy have defects in cardiolipin-stimulated GTP hydrolysis and membrane tubulation. *Hum Mol*
653 *Genet* **19**:2113–2122. doi:10.1093/hmg/ddq088

654 Bonifert T, Karle KN, Tonagel F, Batra M, Wilhelm C, Theurer Y, Schoenfeld C, Kluba T, Kamenisch Y,
655 Carelli V, Wolf J, Gonzalez MA, Speziani F, Schüle R, Züchner S, Schöls L, Wissinger B, Synofzik
656 M. 2014. Pure and syndromic optic atrophy explained by deep intronic OPA1 mutations and an
657 intralocus modifier. *Brain* **137**:2164–2177. doi:10.1093/brain/awu165

658 Bonneau D, Colin E, Oca F, Ferre M, Chevrollier A, Guéguen N, Desquiret-Dumas V, N'Guyen S, Barth
659 M, Zanlonghi X, Rio M, Desguerre I, Barnerias C, Momtchilova M, Rodriguez D, Slama A, Lenaers
660 G, Procaccio V, Amati-Bonneau P, Reynier P. 2014. Letter to the editor: Early-onset Behr syndrome
661 due to compound heterozygous mutations in OPA1. *Brain* **137**. doi:10.1093/brain/awu184

662 Brand AH, Perrimon N. 1993. Targeted gene expression as a means of altering cell fates and generating
663 dominant phenotypes. *Development* **118**:401–415. doi:10.1242/dev.118.2.401

664 Byrne JJ, Soh MS, Chandhok G, Vijayaraghavan T, Teoh JS, Crawford S, Cobham AE, Yapa NMB, Mirth
665 CK, Neumann B. 2019. Disruption of mitochondrial dynamics affects behaviour and lifespan in
666 Caenorhabditis elegans. *Cell Mol Life Sci* **76**:1967–1985. doi:10.1007/s00018-019-03024-5

667 Carelli V, Musumeci O, Caporali L, Zanna C, La Morgia C, Del Dotto V, Porcelli AM, Rugolo M,
668 Valentino ML, Iommarini L, Maresca A, Barboni P, Carbonelli M, Trombetta C, Valente EM,
669 Patergnani S, Giorgi C, Pinton P, Rizzo G, Tonon C, Lodi R, Avoni P, Liguori R, Baruzzi A, Toscano
670 A, Zeviani M. 2015. Syndromic parkinsonism and dementia associated with OPA1 missense
671 mutations. *Ann Neurol* **78**:21–38. doi:10.1002/ana.24410

672 Chao De La Barca JM, Fogazza M, Rugolo M, Chupin S, Del Dotto V, Ghelli AM, Carelli V, Simard G,
673 Procaccio V, Bonneau D, Lenaers G, Reynier P, Zanna C. 2020. Metabolomics hallmarks OPA1
674 variants correlating with their in vitro phenotype and predicting clinical severity. *Hum Mol Genet*
675 **29**:1319–1329. doi:10.1093/hmg/ddaa047

676 Davies VJ, Hollins AJ, Piechota MJ, Yip W, Davies JR, White KE, Nicols PP, Boulton ME, Votruba M.

677 2007. Opa1 deficiency in a mouse model of autosomal dominant optic atrophy impairs mitochondrial
678 morphology, optic nerve structure and visual function. *Hum Mol Genet* **16**:1307–1318.
679 doi:10.1093/hmg/ddm079

680 Del Dotto V, Carelli V. 2021. Dominant Optic Atrophy (DOA): Modeling the Kaleidoscopic Roles of
681 OPA1 in Mitochondrial Homeostasis. *Front Neurol*. doi:10.3389/fneur.2021.681326

682 Del Dotto V, Fogazza M, Musiani F, Maresca A, Aleo SJ, Caporali L, La Morgia C, Nolli C, Lodi T,
683 Goffrini P, Chan D, Carelli V, Rugolo M, Baruffini E, Zanna C. 2018. Deciphering OPA1 mutations
684 pathogenicity by combined analysis of human, mouse and yeast cell models. *Biochim Biophys Acta -*
685 *Mol Basis Dis* **1864**:3496–3514. doi:10.1016/j.bbadis.2018.08.004

686 Del Dotto V, Mishra P, Vidoni S, Fogazza M, Maresca A, Caporali L, McCaffery JM, Cappelletti M,
687 Baruffini E, Lenaers G, Chan D, Rugolo M, Carelli V, Zanna C. 2017. OPA1 Isoforms in the
688 Hierarchical Organization of Mitochondrial Functions. *Cell Rep* **19**:2557–2571.
689 doi:10.1016/j.celrep.2017.05.073

690 Delettre C, Lenaers G, Griffoin JM, Gigarel N, Lorenzo C, Belenguer P, Pelloquin L, Grosgeorge J, Turc-
691 Carel C, Perret E, Astarie-Dequeker C, Lasquellec L, Arnaud B, Ducommun B, Kaplan J, Hamel CP.
692 2000. Nuclear gene OPA1, encoding a mitochondrial dynamin-related protein, is mutated in dominant
693 optic atrophy. *Nat Genet* **26**:207–210. doi:10.1038/79936

694 Deng H, Dodson MW, Huang H, Guo M. 2008. The Parkinson's disease genes pink1 and parkin promote
695 mitochondrial fission and/or inhibit fusion in Drosophila. *Proc Natl Acad Sci U S A* **105**:14503–
696 14508. doi:10.1073/pnas.0803998105

697 Eijkenboom I, Vanoevelen JM, Hoeijmakers JGJ, Wijnen I, Gerards M, Faber CG, Smeets HJM. 2019. A
698 zebrafish model to study small-fiber neuropathy reveals a potential role for GDAP1. *Mitochondrion*
699 **47**:273–281. doi:10.1016/j.mito.2019.01.002

700 Esser K, Tursun B, Ingenhoven M, Michaelis G, Pratje E. 2002. A novel two-step mechanism for removal
701 of a mitochondrial signal sequence involves the mAAA complex and the putative rhomboid protease
702 Pcp1. *J Mol Biol* **323**:835–843. doi:10.1016/S0022-2836(02)01000-8

703 Faelber K, Dietrich L, Noel JK, Wollweber F, Pfitzner AK, Mühleip A, Sánchez R, Kudryashev M,

704 Chiaruttini N, Lilie H, Schlegel J, Rosenbaum E, Hessenberger M, Matthaeus C, Kunz S, von der
705 Malsburg A, Noé F, Roux A, van der Laan M, Kühlbrandt W, Daumke O. 2019. Structure and
706 assembly of the mitochondrial membrane remodelling GTPase Mgm1. *Nature* **571**:429–433.
707 doi:10.1038/s41586-019-1372-3

708 Ferré M, Caignard A, Milea D, Leruez S, Cassereau J, Chevrollier A, Amati-Bonneau P, Verny C, Bonneau
709 D, Procaccio V, Reynier P. 2015. Improved locus-specific database for OPA1 mutations allows
710 inclusion of advanced clinical data. *Hum Mutat* **36**:20–25. doi:10.1002/humu.22703

711 Fish J, Raule N, Attardi G. 2004. Discovery of a major D-loop replication origin reveals two modes of
712 human mtDNA synthesis. *Science (80-)* **306**:2098–2101. doi:10.1126/science.1102077

713 Frezza C, Cipolat S, Martins de Brito O, Micaroni M, Beznoussenko G V., Rudka T, Bartoli D, Polishuck
714 RS, Danial NN, De Strooper B, Scorrano L. 2006. OPA1 Controls Apoptotic Cristae Remodeling
715 Independently from Mitochondrial Fusion. *Cell* **126**:177–189. doi:10.1016/j.cell.2006.06.025

716 Garesse R, Kaguni LS. 2005. A Drosophila model of mitochondrial DNA replication: Proteins, genes and
717 regulation. *IUBMB Life*. doi:10.1080/15216540500215572

718 Goddard JM, Wolstenholme DR. 1978. Origin and direction of replication in mitochondrial DNA molecules
719 from Drosophila melanogaster. *Proc Natl Acad Sci U S A* **75**:3886–3890. doi:10.1073/pnas.75.8.3886

720 Golic KG, Lindquist S. 1989. The FLP recombinase of yeast catalyzes site-specific recombination in the
721 drosophila genome. *Cell* **59**:499–509. doi:10.1016/0092-8674(89)90033-0

722 Henrie A, Hemphill SE, Ruiz-Schultz N, Cushman B, DiStefano MT, Azzariti D, Harrison SM, Rehm HL,
723 Eilbeck K. 2018. ClinVar Miner: Demonstrating utility of a Web-based tool for viewing and filtering
724 ClinVar data. *Hum Mutat* **39**:1051–1060. doi:10.1002/humu.23555

725 Herlan M, Vogel F, Bornhövd C, Neupert W, Reichert AS. 2003. Processing of Mgm1 by the rhomboid-
726 type protease Pcp1 is required for maintenance of mitochondrial morphology and of mitochondrial
727 DNA. *J Biol Chem* **278**:27781–27788. doi:10.1074/jbc.M211311200

728 Kanazawa T, Zappaterra MD, Hasegawa A, Wright AP, Newman-Smith ED, Buttle KF, McDonald K,
729 Mannella CA, Van Der Bliek AM. 2008. The C. elegans Opa1 homologue EAT-3 is essential for
730 resistance to free radicals. *PLoS Genet* **4**. doi:10.1371/journal.pgen.1000022

731 Kane MS, Alban J, Desquiret-Dumas V, Gueguen N, Ishak L, Ferre M, Amati-Bonneau P, Procaccio V,
732 Bonneau D, Lenaers G, Reynier P, Chevrollier A. 2017. Autophagy controls the pathogenicity of
733 OPA1 mutations in dominant optic atrophy. *J Cell Mol Med* **21**:2284–2297. doi:10.1111/jcmm.13149

734 Lee JJ, Sanchez-Martinez A, Zarate AM, Benincá C, Mayor U, Clague MJ, Whitworth AJ. 2018. Basal
735 mitophagy is widespread in Drosophila but minimally affected by loss of Pink1 or parkin. *J Cell Biol*
736 **217**:1613–1622. doi:10.1083/jcb.201801044

737 Lenaers G, Neutzner A, Le Dantec Y, Jüschke C, Xiao T, Decembrini S, Swirski S, Kieninger S, Agca C,
738 Kim US, Reynier P, Yu-Wai-Man P, Neidhardt J, Wissinger B. 2021. Dominant optic atrophy:
739 Culprit mitochondria in the optic nerve. *Prog Retin Eye Res*. doi:10.1016/j.preteyeres.2020.100935

740 Li D, Wang J, Jin Z, Zhang Z. 2019. Structural and evolutionary characteristics of dynamin-related GTPase
741 OPA1. *PeerJ* **2019**. doi:10.7717/peerj.7285

742 Liesa M, Palacín M, Zorzano A. 2009. Mitochondrial dynamics in mammalian health and disease. *Physiol*
743 *Rev*. doi:10.1152/physrev.00030.2008

744 Liu W, Duan X, Xu L, Shang W, Zhao J, Wang L, Li JC, Chen CH, Liu JP, Tong C. 2020. Chchd2 regulates
745 mitochondrial morphology by modulating the levels of Opa1. *Cell Death Differ* **27**:2014–2029.
746 doi:10.1038/s41418-019-0482-7

747 Lynch DS, Loh SHY, Harley J, Noyce AJ, Martins LM, Wood NW, Houlden H, Plun-Favreau H. 2017.
748 Clinical/Scientific Notes: Nonsyndromic Parkinson disease in a family with autosomal dominant
749 optic atrophy due to opa1 mutations. *Neurol Genet* **3**. doi:10.1212/NXG.0000000000000188

750 MacVicar T, Langer T. 2016. OPA1 processing in cell death and disease - the long and short of it. *J Cell*
751 *Sci*. doi:10.1242/jcs.159186

752 McQuibban GA, Lee JR, Zheng L, Juusola M, Freeman M. 2006. Normal Mitochondrial Dynamics
753 Requires Rhomboid-7 and Affects Drosophila Lifespan and Neuronal Function. *Curr Biol* **16**:982–
754 989. doi:10.1016/j.cub.2006.03.062

755 Meglei G, McQuibban GA. 2009. The dynamin-related protein Mgm1p assembles into oligomers and
756 hydrolyzes GTP to function in mitochondrial membrane fusion. *Biochemistry* **48**:1774–1784.
757 doi:10.1021/bi801723d

758 Newsome TP, Åsling B, Dickson BJ. 2000a. Analysis of Drosophila photoreceptor axon guidance in eye-
759 specific mosaics. *Development* **127**:851–860. doi:10.1242/dev.127.4.851

760 Newsome TP, Schmidt S, Dietzl G, Keleman K, Åsling B, Debant A, Dickson BJ. 2000b. Trio combines
761 with dock to regulate Pak activity during photoreceptor axon pathfinding in Drosophila. *Cell*
762 **101**:283–294. doi:10.1016/S0092-8674(00)80838-7

763 Nguyen D, Alavi M V., Kim KY, Kang T, Scott RT, Noh YH, Lindsey JD, Wissinger B, Ellisman MH,
764 Weinreb RN, Perkins GA, Ju WK. 2011. A new vicious cycle involving glutamate excitotoxicity,
765 oxidative stress and mitochondrial dynamics. *Cell Death Dis* **2**. doi:10.1038/cddis.2011.117

766 Nitta Y, Kawai H, Maki R, Osaka J, Hakeda-Suzuki S, Nagai Y, Doubková K, Uehara T, Watanabe K,
767 Kosaki K, Suzuki T, Tavosanis G, Sugie A. 2023. Direct evaluation of neuroaxonal degeneration
768 with the causative genes of neurodegenerative diseases in Drosophila using the automated axon
769 quantification system, MeDUsA . *Hum Mol Genet*. doi:10.1093/hmg/ddac307

770 Olichon A, ElAchouri G, Baricault L, Delettre C, Belenguer P, Lenaers G. 2007. OPA1 alternate splicing
771 uncouples an evolutionary conserved function in mitochondrial fusion from a vertebrate restricted
772 function in apoptosis. *Cell Death Differ* **14**:682–692. doi:10.1038/sj.cdd.4402048

773 Olichon A, Emorine LJ, Descoins E, Pelloquin L, Brichese L, Gas N, Guillou E, Delettre C, Valette A,
774 Hamel CP, Ducommun B, Lenaers G, Belenguer P. 2002. The human dynamin-related protein OPA1
775 is anchored to the mitochondrial inner membrane facing the inter-membrane space. *FEBS Lett*
776 **523**:171–176. doi:10.1016/S0014-5793(02)02985-X

777 Olichon A, Guillou E, Delettre C, Landes T, Arnauné-Pelloquin L, Emorine LJ, Mils V, Daloyau M, Hamel
778 C, Amati-Bonneau P, Bonneau D, Reynier P, Lenaers G, Belenguer P. 2006. Mitochondrial dynamics
779 and disease, OPA1. *Biochim Biophys Acta - Mol Cell Res*. doi:10.1016/j.bbamcr.2006.04.003

780 Poole AC, Thomas RE, Yu S, Vincow ES, Pallanck L. 2010. The mitochondrial fusion-promoting factor
781 mitofusin is a substrate of the PINK1/parkin pathway. *PLoS One* **5**.
782 doi:10.1371/journal.pone.0010054

783 Powell BL, Toomes C, Scott S, Yeung A, Marchbank NJ, Spry PGD, Lumb R, Inglehearn CF, Churchill
784 AJ. 2003. Polymorphisms in OPA1 are associated with normal tension glaucoma. *Mol Vis* **9**:460–464.

785 Rahn JJ, Stackley KD, Chan SSL. 2013. Opa1 Is Required for Proper Mitochondrial Metabolism in Early
786 Development. *PLoS One* **8**. doi:10.1371/journal.pone.0059218

787 Rice P, Longden L, Bleasby A. 2000. EMBOSS: The European Molecular Biology Open Software Suite.
788 *Trends Genet* **16**:276–277. doi:10.1016/S0168-9525(00)02024-2

789 Richard M, Doubková K, Nitta Y, Kawai H, Sugie A, Tavosanis G. 2022. A Quantitative Model of Sporadic
790 Axonal Degeneration in the Drosophila Visual System. *J Neurosci* **42**:4937–4952.
791 doi:10.1523/JNEUROSCI.2115-21.2022

792 Rolland SG, Lu Y, David CN, Conradt B. 2009. The BCL-2-like protein CED-9 of C. elegans promotes
793 FZO-1/Mfn1,2- and EAT-3/Opa1-dependent mitochondrial fusion. *J Cell Biol* **186**:525–540.
794 doi:10.1083/jcb.200905070

795 Rubenstein JLR, Brutlag D, Clayton DA. 1977. The mitochondrial DNA of drosophila melanogaster exists
796 in two distinct and stable superhelical forms. *Cell* **12**:471–482. doi:10.1016/0092-8674(77)90123-4

797 Rujiviphat J, Meglei G, Rubinstein JL, McQuibban GA. 2009. Phospholipid association is essential for
798 dynamin-related protein Mgm1 to function in mitochondrial membrane fusion. *J Biol Chem*
799 **284**:28682–28686. doi:10.1074/jbc.M109.044933

800 Sandoval H, Yao CK, Chen K, Jaiswal M, Donti T, Lin YQ, Bayat V, Xiong B, Zhang K, David G, Charng
801 WL, Yamamoto S, Duraine L, Graham BH, Bellen HJ. 2014. Mitochondrial fusion but not fission
802 regulates larval growth and synaptic development through steroid hormone production. *Elife* **3**:1–23.
803 doi:10.7554/eLife.03558

804 Sanes JR, Zipursky SL. 2020. Synaptic Specificity, Recognition Molecules, and Assembly of Neural
805 Circuits. *Cell*. doi:10.1016/j.cell.2020.04.008

806 Sanes JR, Zipursky SL. 2010. Design Principles of Insect and Vertebrate Visual Systems. *Neuron*.
807 doi:10.1016/j.neuron.2010.01.018

808 Sarzi E, Angebault C, Seveno M, Gueguen N, Chaix B, Bielicki G, Boddaert N, Mausset-Bonnefont AL,
809 Cazevieille C, Rigau V, Renou JP, Wang J, Delettre C, Brabet P, Puel JL, Hamel CP, Reynier P,
810 Lenaers G. 2012. The human OPA1delTTAG mutation induces premature age-related systemic
811 neurodegeneration in mouse. *Brain* **135**:3599–3613. doi:10.1093/brain/aws303

812 Sarzi E, Seveno M, Piro-Mégy C, Elzière L, Quilès M, Péquignot M, Müller A, Hamel CP, Lenaers G,
813 Delettre C. 2018. OPA1 gene therapy prevents retinal ganglion cell loss in a Dominant Optic Atrophy
814 mouse model. *Sci Rep* **8**. doi:10.1038/s41598-018-20838-8

815 Schaaf CP, Blazo M, Lewis RA, Tonini RE, Takei H, Wang J, Wong LJ, Scaglia F. 2011. Early-onset
816 severe neuromuscular phenotype associated with compound heterozygosity for OPA1 mutations. *Mol*
817 *Genet Metab* **103**:383–387. doi:10.1016/j.ymgme.2011.04.018

818 Schindelin J, Arganda-Carreras I, Frise E, Kaynig V, Longair M, Pietzsch T, Preibisch S, Rueden C,
819 Saalfeld S, Schmid B, Tinevez JY, White DJ, Hartenstein V, Eliceiri K, Tomancak P, Cardona A.
820 2012. Fiji: An open-source platform for biological-image analysis. *Nat Methods*.
821 doi:10.1038/nmeth.2019

822 Shahrestani P, Leung HT, Le PK, Pak WL, Tse S, Ocorr K, Huang T. 2009. Heterozygous mutation of
823 Drosophila Opa1 causes the development of multiple organ abnormalities in an age-dependent and
824 organ-specific manner. *PLoS One* **4**. doi:10.1371/journal.pone.0006867

825 Shimizu S, Mori N, Kishi M, Sugata H, Tsuda A, Kubota N. 2003. A novel mutation in the OPA1 gene in
826 a Japanese patient with optic atrophy. *Am J Ophthalmol* **135**:256–257. doi:10.1016/S0002-
827 9394(02)01929-3

828 Sladen PE, Perdigão PRL, Salsbury G, Novoselova T, van der Spuy J, Chapple JP, Yu-Wai-Man P,
829 Cheetham ME. 2021. CRISPR-Cas9 correction of OPA1 c.1334G>A: p.R445H restores
830 mitochondrial homeostasis in dominant optic atrophy patient-derived iPSCs. *Mol Ther - Nucleic*
831 *Acids* **26**:432–443. doi:10.1016/j.omtn.2021.08.015

832 Spiegel R, Saada A, Flannery PJ, Burté F, Soiferman D, Khayat M, Eisner V, Vladovski E, Taylor RW,
833 Bindoff LA, Shaag A, Mandel H, Schuler-Furman O, Shalev SA, Elpeleg O, Yu-Wai-Man P. 2016.
834 Fatal infantile mitochondrial encephalomyopathy, hypertrophic cardiomyopathy and optic atrophy
835 associated with a homozygous OPA1 mutation. *J Med Genet* **53**:127–131. doi:10.1136/jmedgenet-
836 2015-103361

837 Sugie A, Möhl C, Hakeda-Suzuki S, Matsui H, Suzuki T, Tavosanis G. 2017. Analyzing synaptic
838 modulation of drosophila melanogaster photoreceptors after exposure to prolonged light. *J Vis Exp*

839 **2017**. doi:10.3791/55176

840 Tang S, Le PK, Tse S, Wallace DC, Huang T. 2009. Heterozygous mutation of Opa1 in Drosophila shortens
841 lifespan mediated through increased reactive oxygen species production. *PLoS One* **4**.
842 doi:10.1371/journal.pone.0004492

843 Toomes C, Marchbank NJ, Mackey DA, Craig JE, Newbury-Ecob RA, Bennett CP, Vize CJ, Desai SP,
844 Black GCM, Patel N, Teimory M, Markham AF, Inglehearn CF, Churchill AJ. 2001. Spectrum,
845 frequency and penetrance of OPA1 mutations in dominant optic atrophy. *Hum Mol Genet* **10**:1369–
846 1378. doi:10.1093/hmg/10.13.1369

847 Trevisan T, Pendin D, Montagna A, Bova S, Ghelli AM, Daga A. 2018. Manipulation of Mitochondria
848 Dynamics Reveals Separate Roles for Form and Function in Mitochondria Distribution. *Cell Rep*
849 **23**:1742–1753. doi:10.1016/j.celrep.2018.04.017

850 Tsuyama T, Tsubouchi A, Usui T, Imamura H, Uemura T. 2017. Mitochondrial dysfunction induces
851 dendritic loss via eIF2α phosphorylation. *J Cell Biol* **216**:815–834. doi:10.1083/jcb.201604065

852 Vagnoni A, Bullock SL. 2016. A simple method for imaging axonal transport in aging neurons using the
853 adult Drosophila wing. *Nat Protoc* **11**:1711–1723. doi:10.1038/nprot.2016.112

854 Verny C, Loiseau D, Scherer C, Lejeune P, Chevrollier A, Gueguen N, Guillet V, Dubas F, Reynier P,
855 Amati-Bonneau P, Bonneau D. 2008. Multiple sclerosis-like disorder in OPA1-related autosomal
856 dominant optic atrophy. *Neurology* **70**:1152–1153. doi:10.1212/01.wnl.0000289194.89359.a1

857 Wang JT, Medress ZA, Barres BA. 2012. Axon degeneration: Molecular mechanisms of a self-destruction
858 pathway. *J Cell Biol*. doi:10.1083/jcb.201108111

859 Whitworth AJ, Lee JR, Ho VMW, Flick R, Chowdhury R, McQuibban GA. 2008. Rhomboid-7 and
860 HtrA2/Omi act in a common pathway with the Parkinson's disease factors Pink1 and Parkin. *DMM*
861 *Dis Model Mech* **1**:168–174. doi:10.1242/dmm.000109

862 Yamada M, Nitta Y, Uehara T, Suzuki H, Miya F, Takenouchi T, Tamura M, Ayabe S, Yoshiki A, Maeno
863 A, Saga Y, Furuse T, Yamada I, Okamoto N, Kosaki K, Sugie A. 2023. Heterozygous loss-of-
864 function DHX9 variants are associated with neurodevelopmental disorders: Human genetic and
865 experimental evidences. *Eur J Med Genet* **66**:104804. doi:10.1016/j.ejmg.2023.104804

866 Yang L, Tang H, Lin X, Wu Y, Zeng S, Pan Y, Li Y, Xiang G, Lin YF, Zhuang SM, Song Z, Jiang Y, Liu
867 X. 2020. OPA1-Exon4b Binds to mtDNA D-Loop for Transcriptional and Metabolic Modulation,
868 Independent of Mitochondrial Fusion. *Front Cell Dev Biol* **8**. doi:10.3389/fcell.2020.00180

869 Yarosh W, Monserrate J, Tong JJ, Tse S, Le PK, Nguyen K, Brachmann CB, Wallace DC, Huang T. 2008.
870 The molecular mechanisms of OPA1-mediated optic atrophy in Drosophila model and prospects for
871 antioxidant treatment. *PLoS Genet* **4**:0062–0071. doi:10.1371/journal.pgen.0040006

872 Yu-Wai-Man P, Griffiths PG, Gorman GS, Lourenco CM, Wright AF, Auer-Grumbach M, Toscano A,
873 Musumeci O, Valentino ML, Caporali L, Lamperti C, Tallaksen CM, Duffey P, Miller J, Whittaker
874 RG, Baker MR, Jackson MJ, Clarke MP, Dhillon B, Czermin B, Stewart JD, Hudson G, Reynier P,
875 Bonneau D, Marques W, Lenaers G, McFarland R, Taylor RW, Turnbull DM, Votruba M, Zeviani
876 M, Carelli V, Bindoff LA, Horvath R, Amati-Bonneau P, Chinnery PF. 2010a. Multi-system
877 neurological disease is common in patients with OPA1 mutations. *Brain* **133**:771–786.
878 doi:10.1093/brain/awq007

879 Yu-Wai-Man P, Spyropoulos A, Duncan HJ, Guadagno J V., Chinnery PF. 2016. A multiple sclerosis-like
880 disorder in patients with OPA1 mutations. *Ann Clin Transl Neurol* **3**:723–729. doi:10.1002/acn3.323

881 Yu-Wai-Man P, Stewart JD, Hudson G, Andrews RM, Griffiths PG, Birch MK, Chinnery PF. 2010b. OPA1
882 increases the risk of normal but not high tension glaucoma. *J Med Genet* **47**:120–125.
883 doi:10.1136/jmg.2009.067512

884 Zaninello M, Palikaras K, Naon D, Iwata K, Herkenne S, Quintana-Cabrera R, Semenzato M, Grespi F,
885 Ross-Cisneros FN, Carelli V, Sadun AA, Tavernarakis N, Scorrano L. 2020. Inhibition of autophagy
886 curtails visual loss in a model of autosomal dominant optic atrophy. *Nat Commun* **11**.
887 doi:10.1038/s41467-020-17821-1

888 Zaninello M, Palikaras K, Sotiriou A, Tavernarakis N, Scorrano L. 2022. Sustained intracellular calcium
889 rise mediates neuronal mitophagy in models of autosomal dominant optic atrophy. *Cell Death Differ*
890 **29**:167–177. doi:10.1038/s41418-021-00847-3

891 Zanna C, Ghelli A, Porcelli AM, Karbowski M, Youle RJ, Schimpf S, Wissinger B, Pinti M, Cossarizza A,
892 Vidoni S, Valentino ML, Rugolo M, Carelli V. 2008. OPA1 mutations associated with dominant

893 optic atrophy impair oxidative phosphorylation and mitochondrial fusion. *Brain* **131**:352–367.
894 doi:10.1093/brain/awm335

895

896 ***Figures with the corresponding legend***

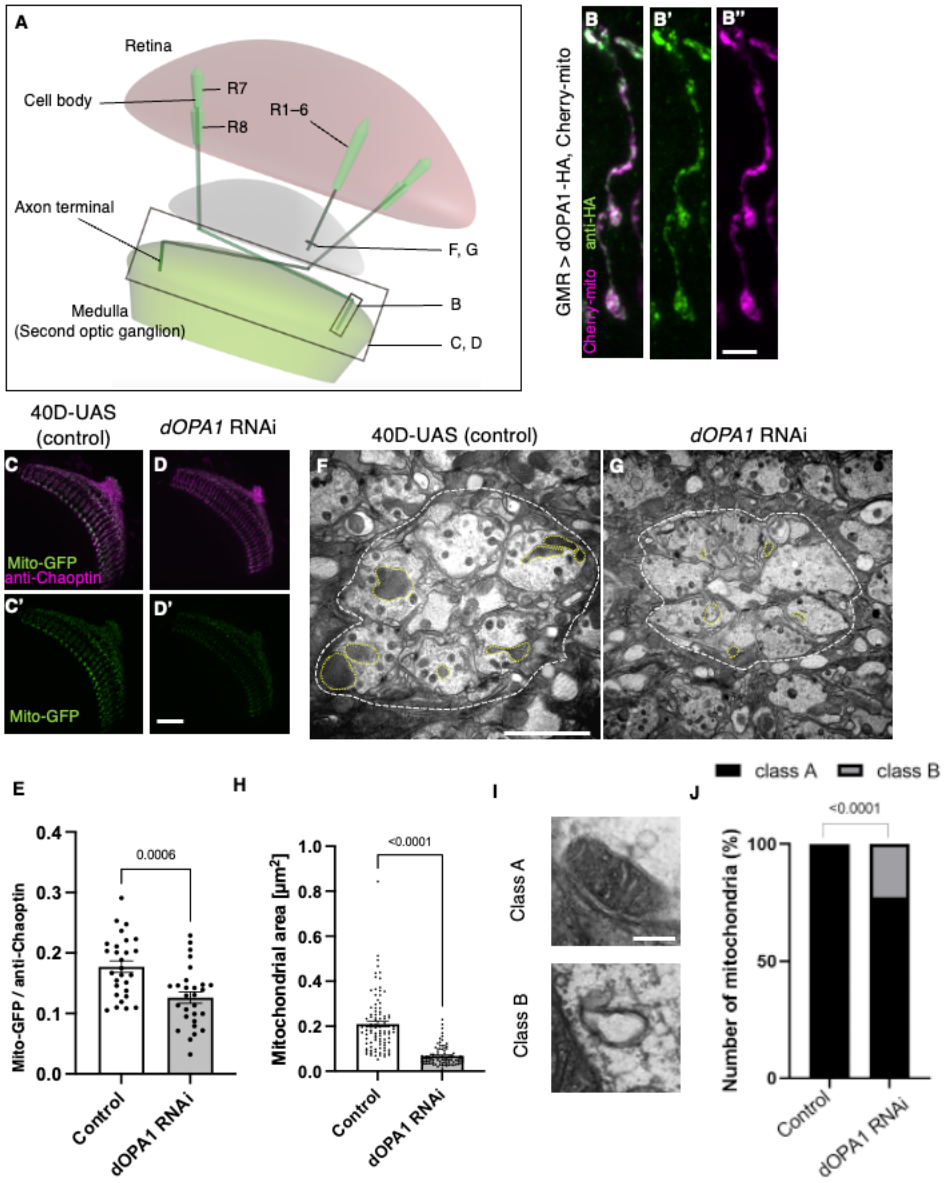

897

898 **Figure 1: Effect of *dOPA1* knockdown on mitochondrial density and size in retinal axons.**

899 (A) Schematic illustration of the *Drosophila* visual system from a dorsal view, highlighting the

900 arrangement of photoreceptor neurons. The rectangular area indicated in B represents a single R7/8
901 photoreceptor axon, as illustrated in the figure for B. The rectangular areas highlighted in C and D
902 encompass the entirety of R7/8 photoreceptor axons, as shown in the figures for C and D. The lines
903 marked in F and G denote cross-sections of R1–6 photoreceptor axons, as depicted in the figures for
904 F and G. (B) Visualization of mitochondria and dOPA1 in a set of R7/8 axons. Mitochondria were
905 visualized using the expression of *mCherry-mito* driven by *GMR-Gal4* (magenta) while HA-tagged
906 dOPA1 was immunostained using the anti-HA antibody (green). Scale bar: 3 μm. (C, D)
907 Representations of mitochondria visualized using the expression of *Mito-GFP* driven by *GMR-Gal4*
908 (green), one day after eclosion. Retinal axons were labeled using the anti-Chaoptin antibody (magenta).
909 Scale bar: 30 μm. (E) Quantification of Mito-GFP intensity. Mito-GFP levels were calculated by
910 dividing the Mito-GFP fluorescence intensity by the anti-Chaoptin signal intensity. Control (n = 28
911 optic lobes) and *dOPA1* RNAi (n = 28 optic lobes). The data are presented as mean ± SEM. (F, G)
912 Electron micrographs of cross sections of the R1–6 retinal axons in the lamina of the Control (F) and
913 d*OPA1* knockdown (G) on the day of eclosion. Yellow circles and white dotted lines indicate
914 mitochondria and a lamina column, respectively. Scale bar: 2 μm. (H) Quantification of the
915 mitochondrial area. Control (n = 96 mitochondria) and *dOPA1* RNAi (n = 92 mitochondria). Data are
916 expressed as mean ± SEM. (I) Representative EM images showing mitochondria with a densely
917 packed matrix structure (classified as class A) and collapsed mitochondria (classified as class B). Scale
918 bar: 500 nm. (J) Quantification of the mitochondria classified into class A and class B. Control (n =
919 96 mitochondria) and *dOPA1* RNAi (n = 92 mitochondria). See the Table1 for the genotypes of the
920 *Drosophila* used in the experiments.

921

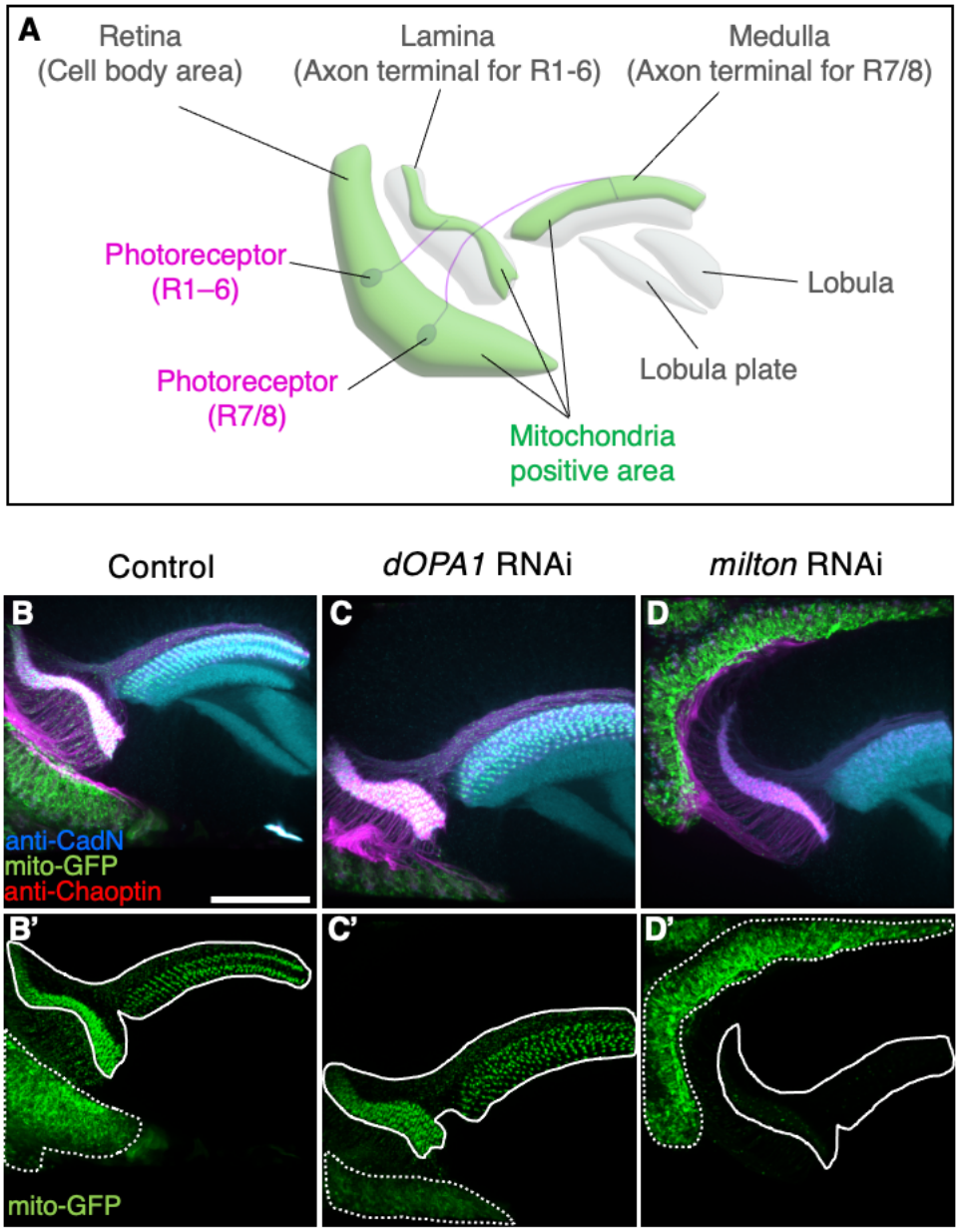

Figure S1. Analysis of trafficking defects in axons of *dOPA1* knockdown flies.

Schematic illustration of the *Drosophila* visual system around 24 h after puparium formation. The cell bodies of photoreceptors (magenta) are found in the retina; type 1–6 photoreceptors project their axons to the lamina of the primary optic ganglion. The axons of type 7/8 photoreceptors project into the medulla of the secondary optic ganglion. Mitochondria are abundantly located in their cell bodies and axon terminals (green). Higher-order visual centers include the lobula and lobula plate. (B–D)

929 Neuropil and photoreceptor cells were labeled using an anti-CadN antibody (cyan) and anti-Chaoptin
930 antibody (magenta), respectively. Mitochondria were visualized using the expression of Mito-GFP
931 driven by *GMR-Gal4* (green). (B, B') and (C, C') show whole photoreceptors in the RNAi Control and
932 *dOPA1* knockdown, respectively. The regions indicated by dashed and solid lines in (B', C', D') indicate
933 the cell body and axonal areas, respectively. (D, D') shows whole photoreceptors in *milton* knockdown.
934 Scale bar: 50 μm. See the Table1 for the genotypes of the *Drosophila* used in the experiments.

935

936

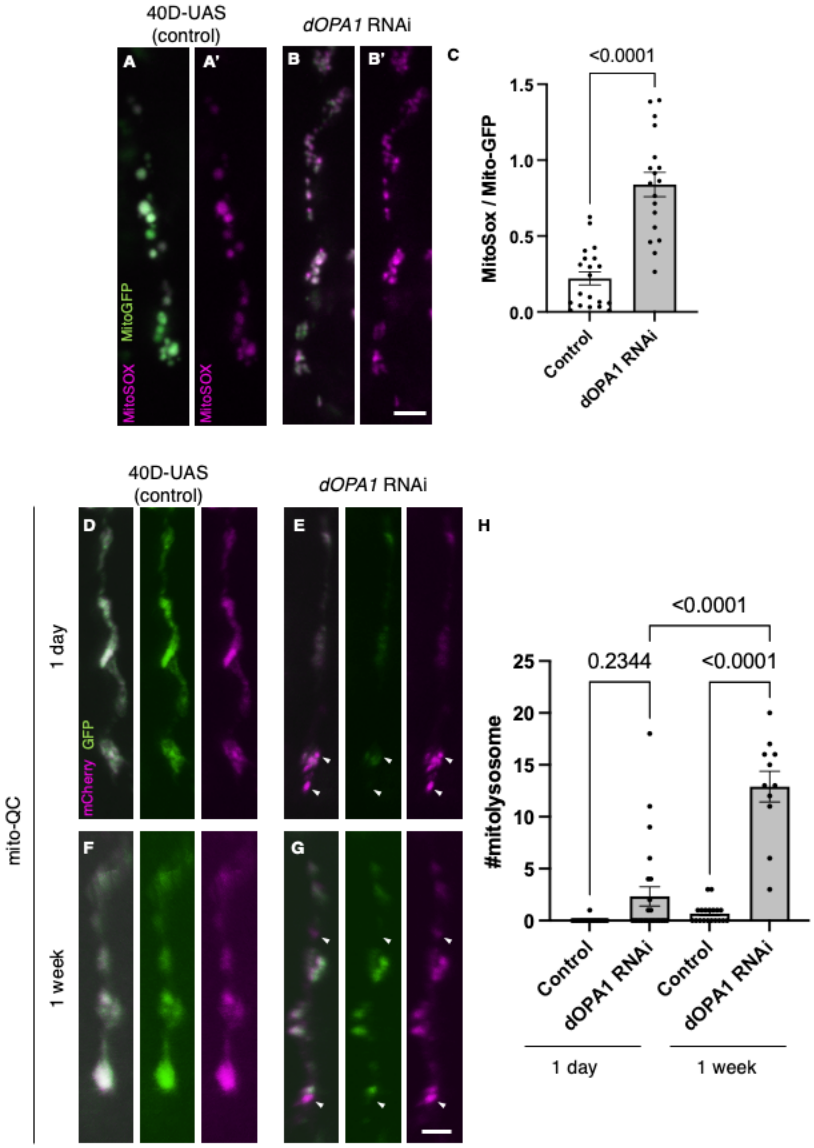

Figure 2. elevated reactive oxygen species and mitophagy activity levels in the *dOPA1* knockdown.

(A, B) Mitochondrial reactive oxygen species (ROS) levels in a set of the R7/8 retinal axon visualized using Mito-GFP (green) driven by *GMR-Gal4* and MitoSOX (magenta) to specifically detect superoxide, an indicator of oxidative stress. Representative images of a retinal axon in the Control (A, A') and *dOPA1* knockdown (B, B'). (C) Quantification of ROS levels for each genotype. ROS levels were determined by dividing the fluorescence intensity of MitoSOX by that of Mito-GFP, highlighting the significant increase in ROS levels in *dOPA1* knockdown flies compared to controls, suggesting

946 enhanced mitochondrial stress and dysfunction upon *dOPA1* depletion. Control (n = 20 optic lobes)
947 and *dOPA1* RNAi (n = 18 optic lobes). Scale bar: 3 μm. Data are presented as mean ± SEM. (D, E)
948 Mitophagy activity in a set of the R7/8 retinal axon visualized by a genetic marker, mito-QC, driven
949 by *GMR-Gal4*. Representative images of a retinal axon in the Control 1 day after eclosion (D), *dOPA1*
950 knockdown 1 day after eclosion (E), the Control 1 week after eclosion (F), *dOPA1* knockdown 1 week
951 after eclosion (G). The arrowheads indicate a mitolysosome that is positive for mCherry and negative
952 for GFP. (H) Quantification of the mitophagy activity each genotype. The number of the
953 mitolysosomes were counted in each genotype. The significant increase in the number of the
954 mitolysosomes in *dOPA1* knockdown flies compared to controls after 1 week, suggesting enhanced
955 mitophagy upon *dOPA1* depletion. Control 1d (n = 18 optic lobes), Control 1week (n = 19 optic lobe),
956 *dOPA1* RNAi 1d (n = 24 optic lobes), and *dOPA1* RNAi 1 week (n = 11 optic lobes). Scale bar: 3 μm.
957 Data are presented as mean ± SEM. See the Table1 for the genotypes of the *Drosophila* used in the
958 experiments.

959

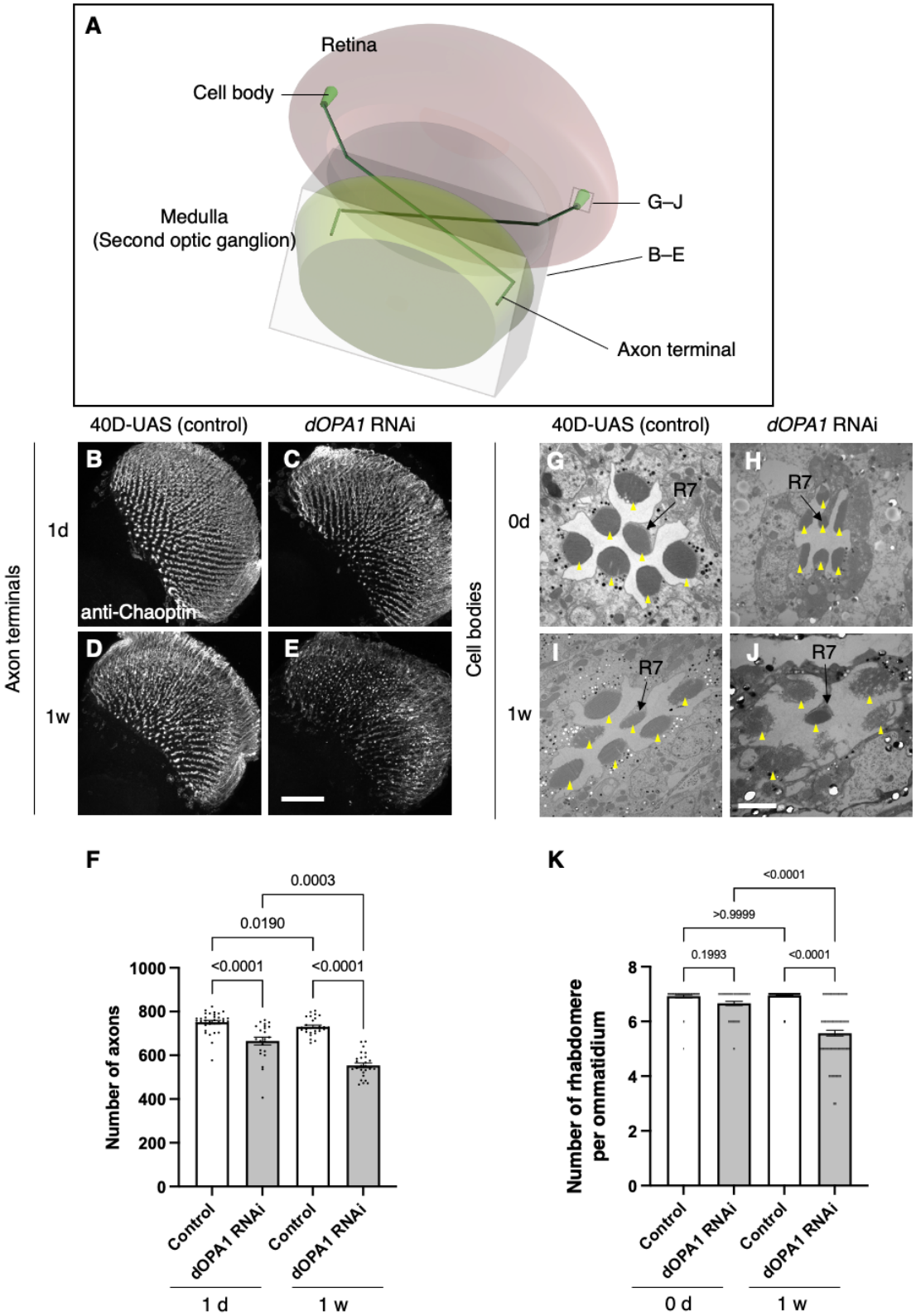

960

961 **Figure 3. Effect of *dOPA1* knockdown on photoreceptor neurodegeneration in *Drosophila*.**

962 Schematic of the visual system in *Drosophila*. A set of R7/8 photoreceptors project their axons to the
963 second optic ganglion medulla. The rectangular prism indicated in B–E represents the area of the
964 whole medulla, as shown in the figure for B–E. The squire marked in G–J denote cross-sections of the
965 cell bodies of the photoreceptors, as depicted in the figures for G–J. (B–E) All R7 and R8 axon
966 terminals project to the medulla. *dOPA1* in the photoreceptor was knocked down by *GMR-Gal4*. *40D-*
967 *UAS* was used as a Control to match the number of *UAS* sequences recognized by Gal4. One day after
968 eclosion in Control (B) and *dOPA1* knockdown (C), and one week after in Control (D) and *dOPA1*
969 knockdown (E). The retinal axons were stained with anti-Chaoptin, a photoreceptor-specific antibody.
970 Scale bar = 50 μm. (F) Number of axons at each time point in R7 neurons for each situation quantified
971 by MeDUsA. At 1 day of Control (n = 34 optic lobes) and *dOPA1* RNAi (n = 23 optic lobes), and at 1
972 week of Control (n = 28 optic lobes) and *dOPA1* RNAi (n = 26 optic lobes). Data are expressed as
973 mean ± SEM. (G–J) Electron micrographs of cross sections of the photoreceptor cell bodies in the
974 ommatidia of the retina. Rhabdomeres are shown as yellow arrowheads. The day of eclosion in Control
975 **(**G**)** and *dOPA1* knockdown (H), and 1-week-old adults of Control (I) and *dOPA1* knockdown (J).
976 Scale bar = 2 μm. **(**K**)** Quantification of the number of rhabdomeres for each genotype and time point.
977 At 0 day in Control (n = 50 ommatidia) and *dOPA1* RNAi (n = 127 ommatidia), and at 1 week in
978 Control (n = 50 ommatidia) and *dOPA1* RNAi (n = 117 ommatidia). Data are expressed as mean ±
979 SEM. See the Table1 for the genotypes of the *Drosophila* used in the experiments.

980

981

982

983

984

985

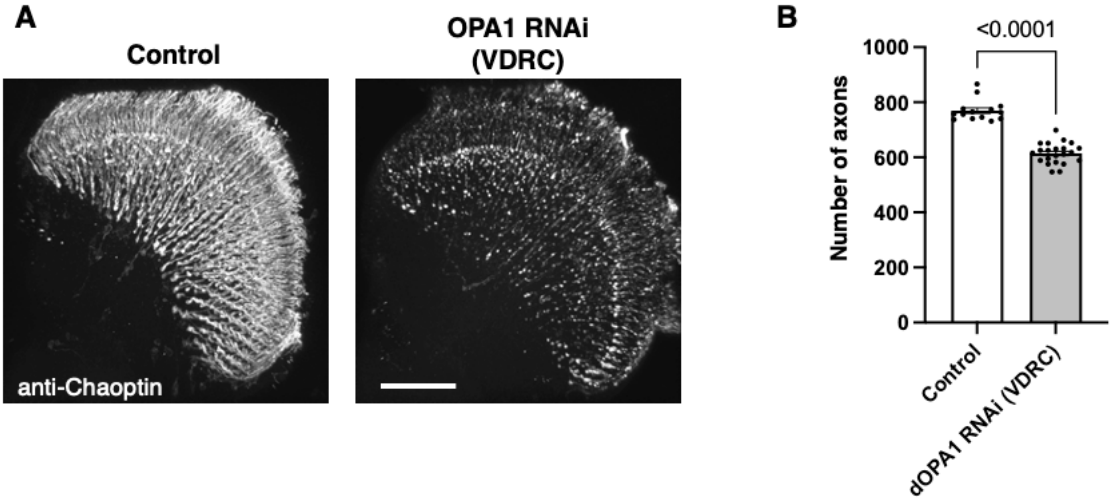

Figure S2. The impact on the retinal axons of another RNAi line in *Drosophila OPA1*.

(A) The images show the representations of retinal axons labeled with an anti-Chaoptin antibody (gray). Control and *dOPA1* RNAi (VDRC 106290) from VDRC two weeks after eclosion. Scale bar: 50 µm. (B) Quantification of the number of axons for each genotype. Control (n = 14 optic lobes) and *dOPA1* RNAi (VDRC 106290) (n = 22 optic lobes). The data are presented as mean ± SEM. See the Table1 for the genotypes of the *Drosophila* used in the experiments.

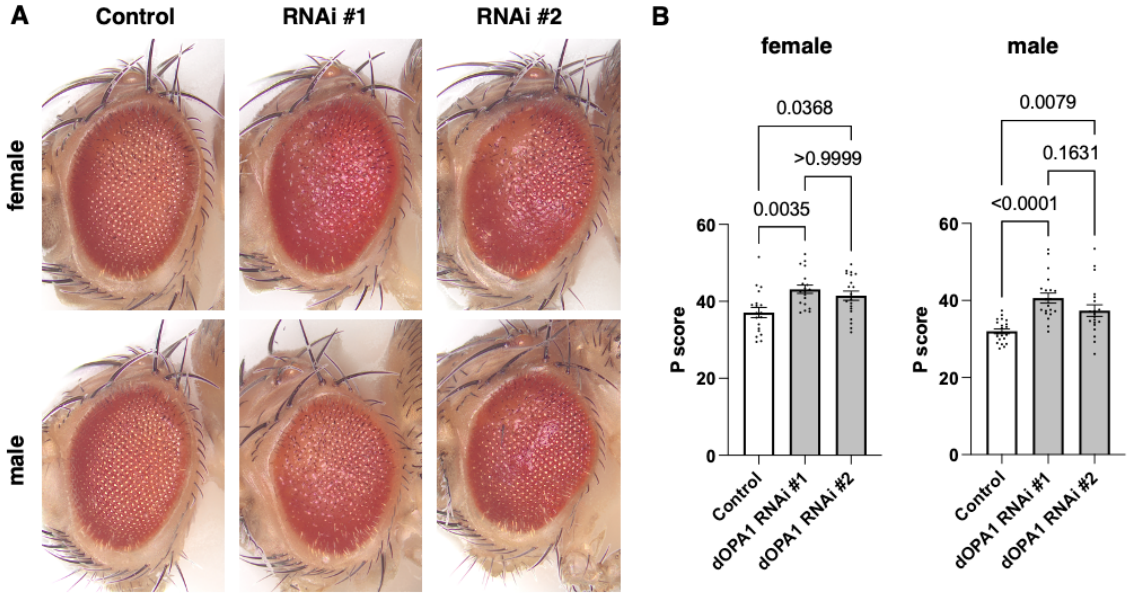

Figure S3. Evaluation of the impact on *Drosophila* compound eyes due to knockdown of *dOPA1*.

(A) Bright-field microscopic images of representative fly eyes expressing 40D-UAS (control), RNAi #1 (BDSC 32358), and RNAi #2 (VDRC 106290) using the *GMR-Gal4* driver. (B) Graph representing the P score of each genotype: female *control* (n = 19), *female RNAi #1* (n = 19), *female RNAi #2* (n = 20), male control (n = 21), *male RNAi #1* (n = 20), and *male RNAi #2* (n = 20). See the Table1 for the genotypes of the *Drosophila* used in the experiments.

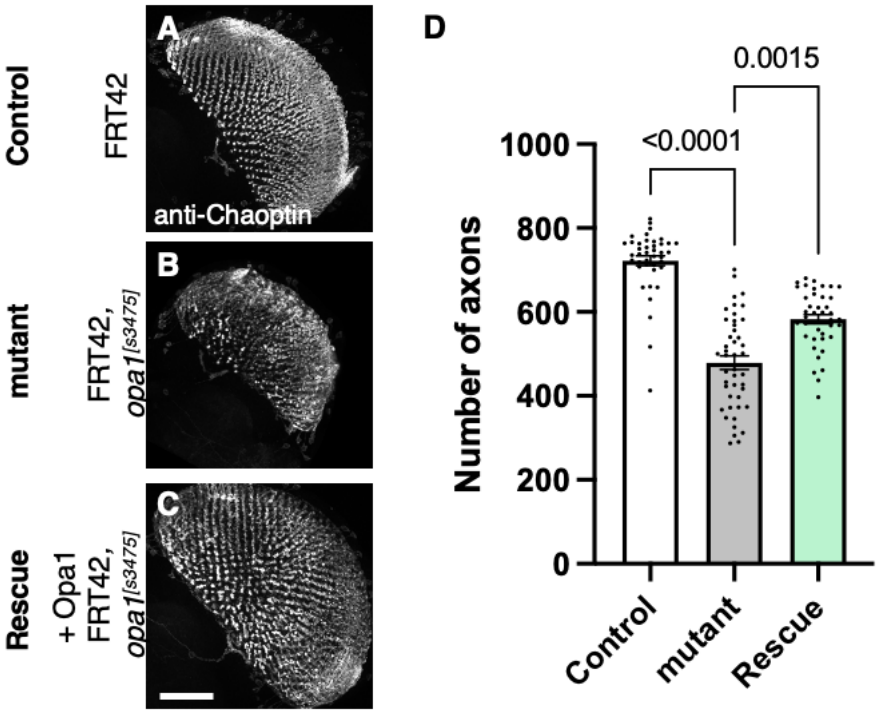

Figure 4. Role of *dOPA1* in the retinal axon according to mutant analysis.

(A–C) Representations of retinal axons labeled with an anti-Chaoptin antibody (gray), one day after eclosion. The images show Control (A), *dOPA1*^{s3475} somatic mosaic flies (B), and *dOPA1*^{s3475} somatic mosaic flies expressing the eye-specific full-length *dOPA1* (C). Scale bar: 50 µm. (D) Quantification of the number of axons for each genotype. Control (n = 41 optic lobes), mutant (n = 45 optic lobes), and rescue (n = 41 optic lobes). The data are presented as mean ± SEM. See the Table1 for the genotypes of the *Drosophila* used in the experiments.

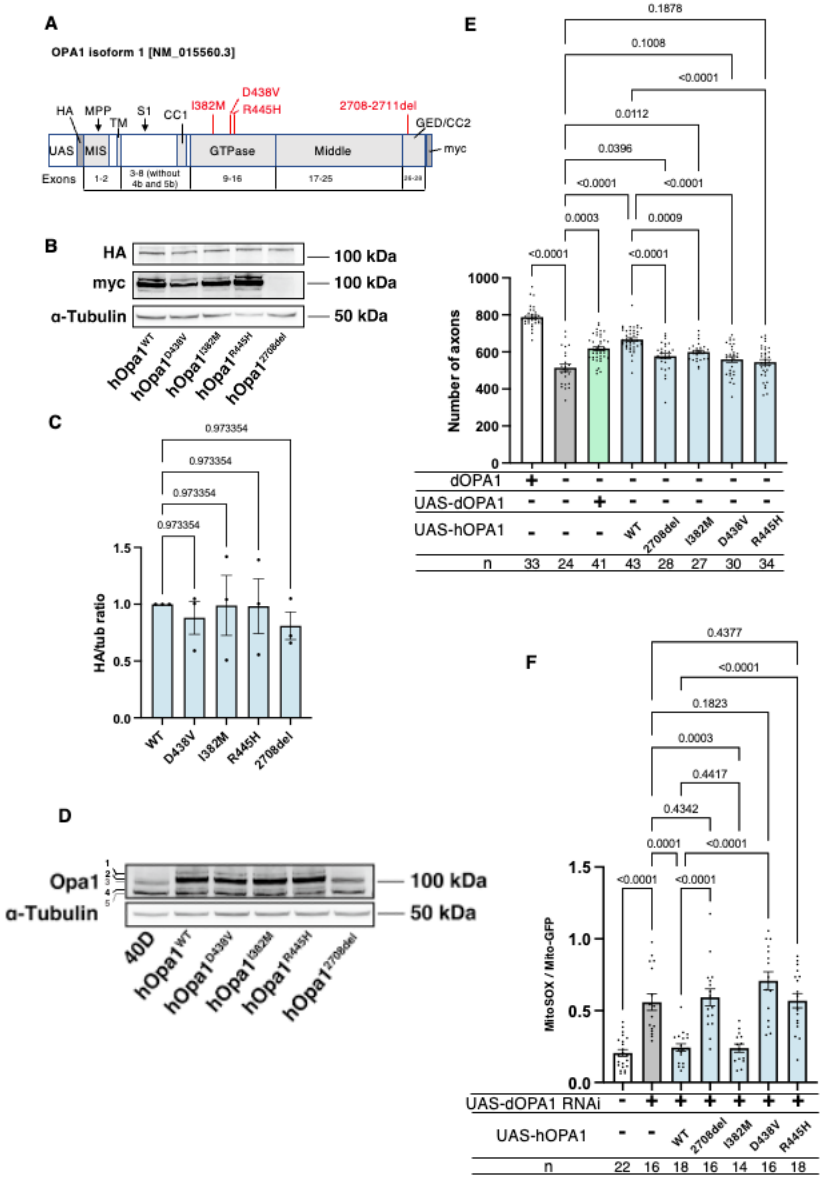

Figure 5. Verification of the pathological significance of disease mutations in *hOPA1*.

(A) Schematic illustration of the *hOPA1* gene construct with HA and myc tags in the UAS-based vector. *hOPA1* includes a mitochondrial import sequence (MIS) cleaved by mitochondrial processing peptidase (MPP), a transmembrane region (TM), a coiled-coil region (CC1), a GTPase domain, a Middle domain, and a GTPase effector domain (GED) containing a coiled-coil region (CC2). The sites

1020 of variants (I382M, D438V, R445H, and a deletion from 2708 to 2711) are shown in red. S1 is the site
1021 cleaved by OMA1. (B) Western blot analysis to confirm the expression of hOPA1 variants.
1022 hOPA1_WT, hOPA1_D438V, hOPA1_I382M, hOPA1_R445H, and hOPA1_2708del were expressed
1023 in whole *Drosophila* bodies and detected using anti-HA and anti-myc antibodies. α-Tubulin was used
1024 as a loading Control. (C) Quantification of the expression levels of the OPA1 protein for each variant.
1025 hOPA1_WT (n = 3), D438V (n = 3), I382M (n = 3), R445H (n = 3), and 2708del (n = 3). The data are
1026 presented as mean ± SEM. (D) Detection of hOPA1 expression in vivo in *Drosophila* using anti-OPA1.
1027 Band 1 represents the full-length OPA1, which includes the MIS, while Band 2 corresponds to the
1028 long-form OPA1 (L-OPA1), cleaved at the MPP. Bands 3 and 5 potentially detect the endogenous
1029 dOPA1. Band 4 is thought to represent the short-form OPA1 (S-OPA1). (E) Rescue experiments were
1030 conducted to assess the expression of each *hOPA1* variant, including *dOPA1*, in the retina axons of
1031 *dOPA1* mutant somatic clones. The sample size is indicated (n). Data are presented as mean ± SEM.
1032 (F) Quantification of mitochondrial ROS levels upon expression of hOPA1 variants in the context of
1033 dOPA1 knockdown. Control (n = 22 optic lobes), *dOPA1* RNAi (n = 16 optic lobes), *hOPA1_WT* with
1034 *dOPA1* RNAi (n = 18 optic lobes) , *hOPA1_2708-2711del* with *dOPA1* RNAi (n = 16 optic lobes),
1035 *hOPA1_I382M* with *dOPA1* RNAi (n = 14 optic lobes), *hOPA1_D438V* with *dOPA1* RNAi (n = 16
1036 optic lobes), and *hOPA1_R445H* with *dOPA1* RNAi (n = 18 optic lobes). Data are presented as mean
1037 ± SEM. See the Table1 for the genotypes of the *Drosophila* used in the experiments.

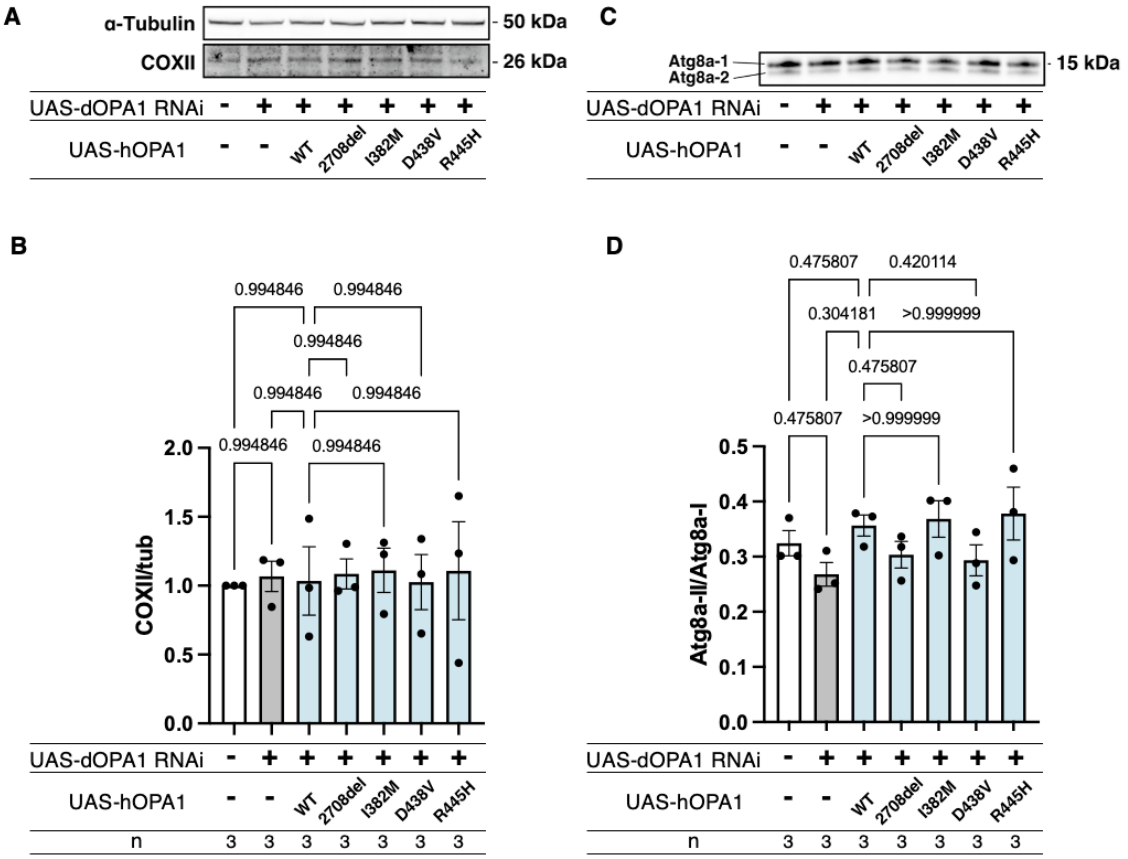

Figure S4. Effects of *hOPA1* variants on COXII expression and Autophagy in the context of *dOPA1* knockdown.

(A) Western blot analysis to show the expression of COXII upon expression of *hOPA1* variants in the context of *dOPA1* knockdown. (B) Quantification of COXII protein levels. Control (n = 3), *luciferase* RNAi with *dOPA1* RNAi (n = 3), *hOPA1_WT* with *dOPA1* RNAi (n = 3) , *hOPA1_2708-2711del* with *dOPA1* RNAi (n = 3), *hOPA1_I382M* with *dOPA1* RNAi (n = 3), *hOPA1_D438V* with *dOPA1* RNAi

1046 (n = 3), and *hOPA1_R445H* with *dOPA1* RNAi (n = 3). Data are presented as mean ± SEM. (C) Western

1047 blot analysis to show the expression of Atg8a-1 and Atg8a-2 upon expression of *hOPA1* variants in the

1048 context of *dOPA1* knockdown. (D) Quantification of the ratio of Atg8a-2 and Atg8a-1. Control (n =

1049 3), luciferase RNAi with *dOPA1* RNAi (n = 3), *hOPA1_WT* with *dOPA1* RNAi (n = 3) , *hOPA1_2708-*

1050 *2711del* with *dOPA1* RNAi (n = 3), *hOPA1_I382M* with *dOPA1* RNAi (n = 3), hOPA1_D438V with

1051 *dOPA1* RNAi (n = 3), and *hOPA1_R445H* with *dOPA1* RNAi (n = 3). Data are presented as mean ±

1052 SEM.

1053

1054

1055

1056

1057

1058

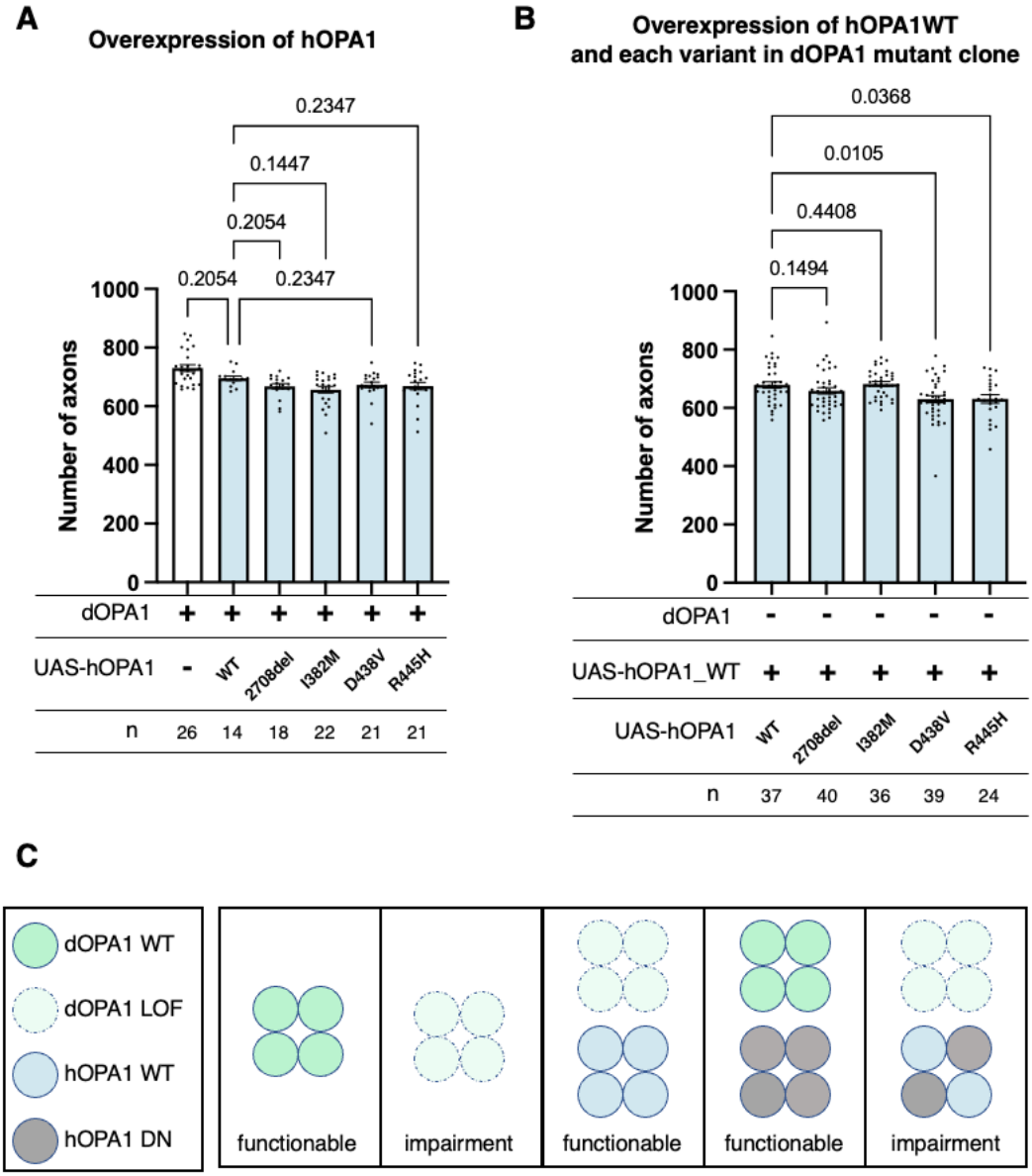

Figure 6. LOF or DN effects of disease mutations in *hOPA1*.

(A) Impact of each human OPA1 variant on the axon number in the optic nerve of *Drosophila* as quantified using MeDUsA. (B) Expression of both *hOPA1* WT and its respective variants was analyzed in photoreceptors lacking *dOPA1*, and the number of axons was quantified using the MeDUsA. The sample size is indicated (n). Data are expressed as mean ± SEM. (C) Schematic representation of

1065 interspecies differences in OPA1 interactions and the interchangeability of OPA1 between human and

1066 fly. See the Table1 for the genotypes of the *Drosophila* used in the experiments.

1067

1068

1069

1070

1071

1072

1073

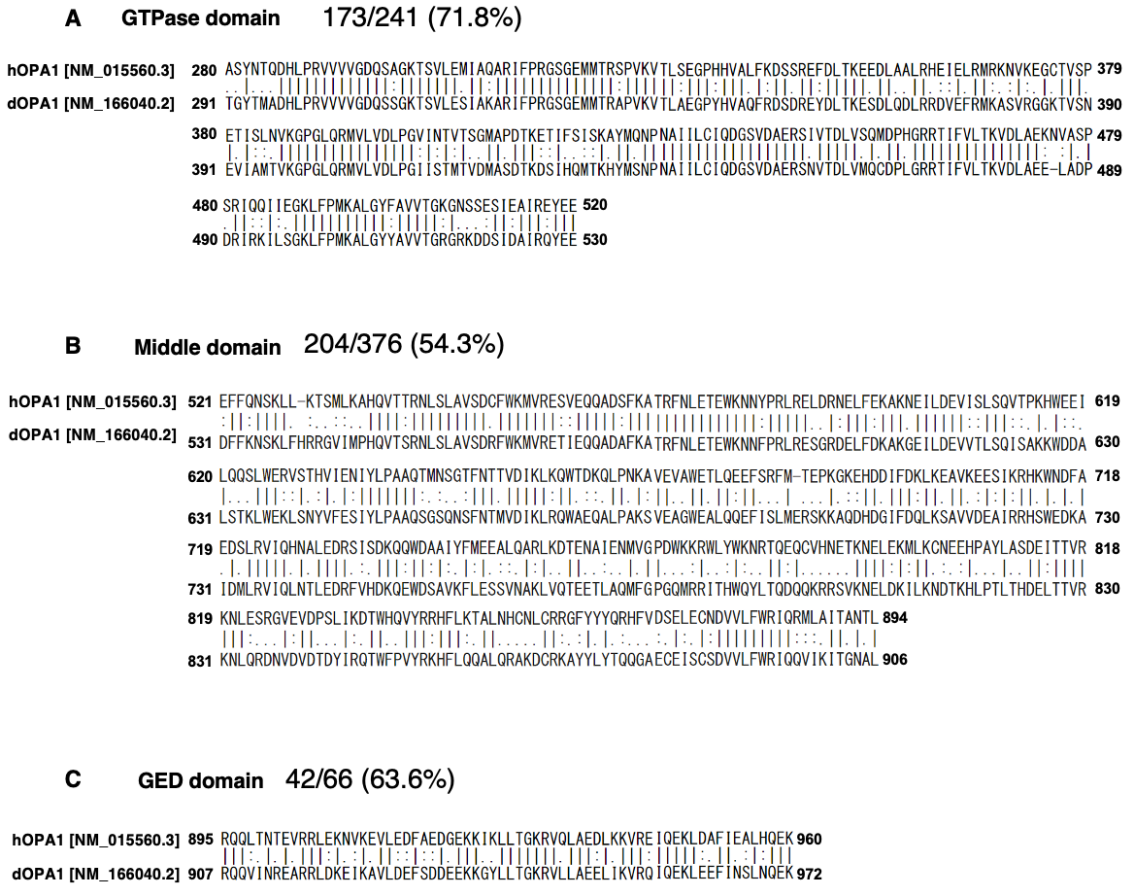

Figure S5. Pairwise Alignment of GTPase, Middle, and GED Domains of hOPA1 and dOPA1.

(A–C) The amino acid sequences of hOPA1 ([NM_015560.3]) and dOPA1 ([NM_166040.2]) were aligned using EMBOSS Needle. GTPase domain (A), Middle domain (B), and GED domain (C). Each percentage value represents the degree of identity within the amino acid sequence. GTPase domain (280–520), Middle domain (521–894), and GED domain (895–907). The beginning and end of each domain were reported previously (Liesa et al., 2009).

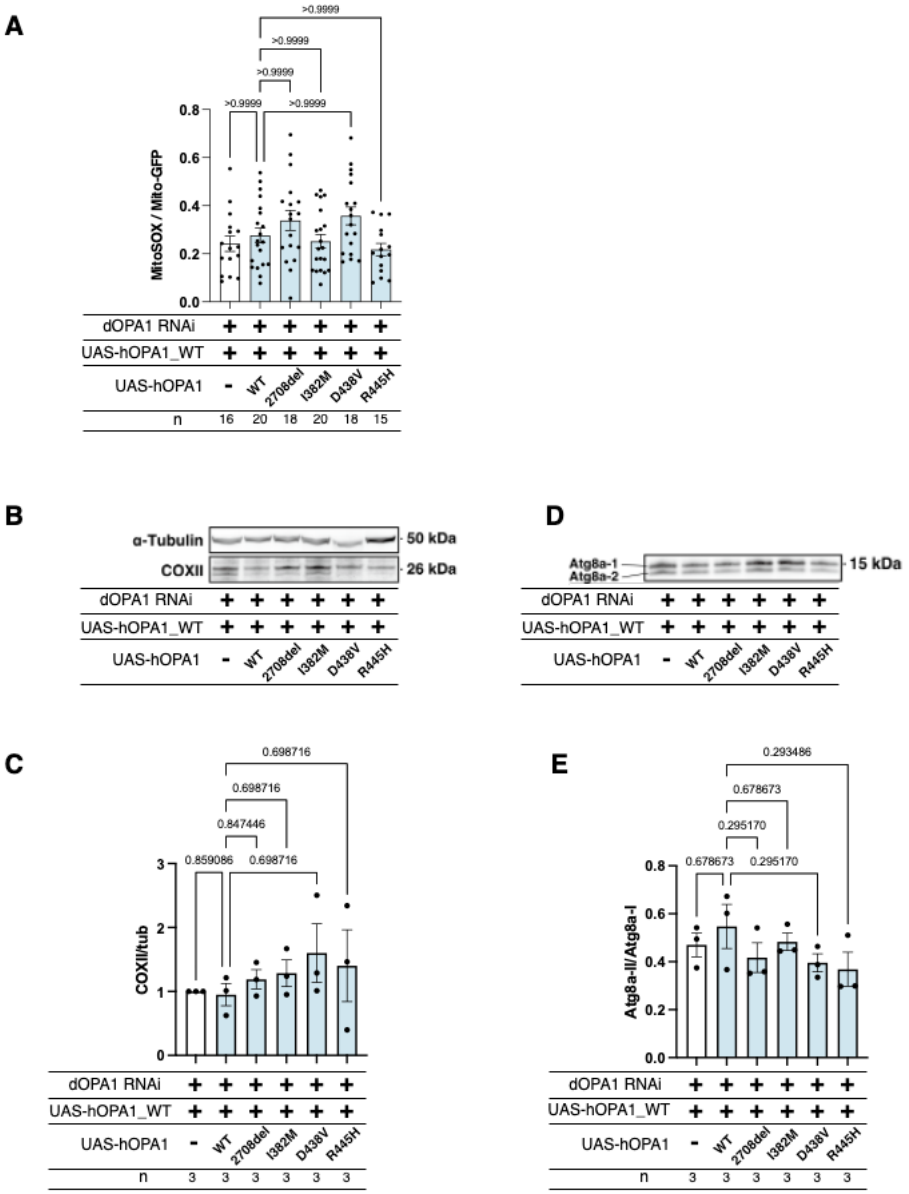

Figure S6. Comparative analysis of mitochondrial ROS levels, COXII expression, and Autophagy between *hOPA1* wild-type and the variants expression under *dOPA1* knockdown conditions.

(A) Impact on mitochondrial ROS levels upon expression of wild-type *hOPA1* and its variants under

conditions of *dOPA1* knockdown. Control (n = 16 optic lobes), *hOPA1_WT* (n = 20 optic lobes) , *hOPA1_2708-2711del* (n = 18 optic lobes), *hOPA1_I382M* (n = 20 optic lobes), *hOPA1_D438V* (n = 18 optic lobes), and *hOPA1_R445H* (n = 15 optic lobes). Data are presented as mean ± SEM. (B) Western blot analysis to show the expression of COXII upon expression of wild-type *hOPA1* and its variants under condition of *dOPA1* knockdown. (C) Quantification of COXII protein levels. Control (n = 3), *hOPA1_WT* (n = 3) , *hOPA1_2708-2711del* (n = 3), *hOPA1_I382M* (n = 3), *hOPA1_D438V* (n = 3), and *hOPA1_R445H* (n = 3). Data are presented as mean ± SEM. (D) Western blot analysis to show the expression of Atg8a-1 and Atg8a-2 upon expression of wild-type *hOPA1* and its variants under condition of *dOPA1* knockdown. (E) Quantification of the ratio of Atg8a-2 and Atg8a-1. Control (n = 3), *hOPA1_WT* (n = 3) , *hOPA1_2708-2711del* (n = 3), *hOPA1_I382M* (n = 3), *hOPA1_D438V* (n = 3), and *hOPA1_R445H* (n = 3). Data are presented as mean ± SEM. See the Table1 for the genotypes of the *Drosophila* used in the experiments.

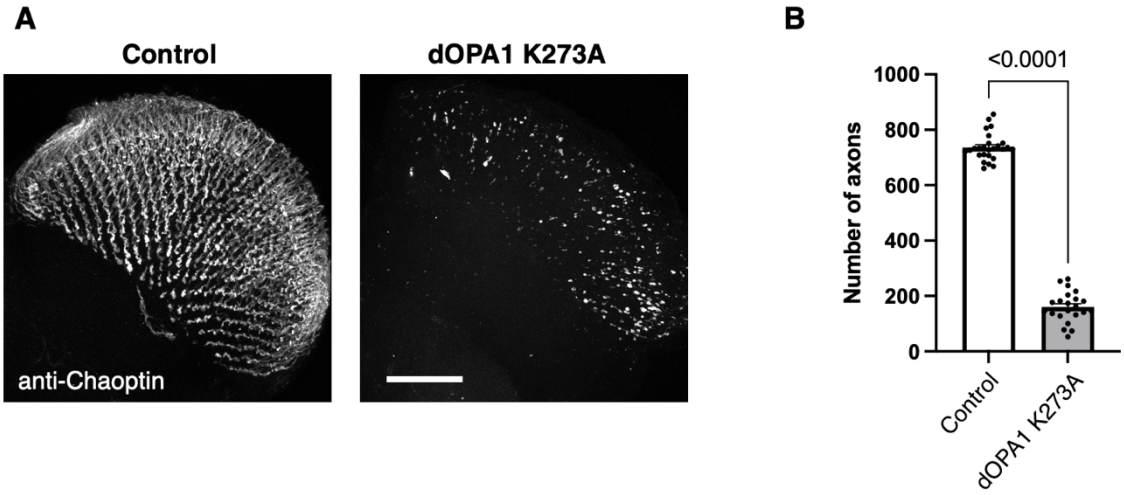

1102

1103 **Figure S7. The effect of a dominant-negative mutation in *dOPA1*.**

1104 (A) The images show the representations of retinal axons labeled with an anti-Chaoptin antibody

1105 (gray). Control and the expression of a presumably GTPase-negative form of $dOPA1^{K273A}$ 1 week after

1106 eclosion. Scale bar: 50 µm. (B) Quantification of the number of axons for each genotype. Control (n

1107 = 26 optic lobes) and $dOPA1^{K273A}$ (n = 22 optic lobes). The data are presented as mean ± SEM. See

1108 the Table1 for the genotypes of the *Drosophila* used in the experiments.

1109